Solid Earth, 4, 23–41, 2013
www.solid-earth.net/4/23/2013/
doi:10.5194/se-4-23-2013

Solid Earth

Reprocessed height time series for GPS stations

S. Rudenko[1], **N. Schön**[1,2], **M. Uhlemann**[1], **and G. Gendt**[1]

[1]Helmholtz Centre Potsdam GFZ German Research Centre for Geosciences, Telegrafenberg, 14473 Potsdam, Germany
[2]Bristol Glaciology Centre, School of Geographical Sciences, University of Bristol, University Road, Bristol BS8 1SS, UK

Correspondence to: S. Rudenko (rudenko@gfz-potsdam.de) and N. Schön (nana.schoen@bristol.ac.uk)

Received: 21 June 2012 – Published in Solid Earth Discuss.: 26 July 2012
Revised: 30 November 2012 – Accepted: 10 December 2012 – Published: 24 January 2013

Abstract. Precise weekly positions of 403 Global Positioning System (GPS) stations located worldwide are obtained by reprocessing GPS data of these stations for the time span from 4 January 1998 until 29 December 2007. The processing algorithms and models used as well as the solution and results obtained are presented. Vertical velocities of 266 GPS stations having a tracking history longer than 2.5 yr are computed; 107 of them are GPS stations located at tide gauges (TIGA observing stations). The vertical velocities calculated in this study are compared with the estimates from the co-located tide gauges and other GPS solutions. The formal errors of the estimated vertical velocities are 0.01–0.80 mm yr^{-1}. The vertical velocities of our solution agree within 1 mm yr^{-1} with those of the recent solutions (ULR5 and ULR3) of the Université de La Rochelle for about 67–75 per cent of the common stations. Examples of typical behaviour of station height changes are given and interpreted. The derived height time series and vertical motions of continuous GPS at tide gauges stations can be used for correcting the vertical land motion in tide gauge records of sea level changes.

1 Introduction

Satellite radar altimetry and tide gauge measurements are the primary techniques for sea level change investigations. Satellite radar altimetry measures absolute sea level using data obtained during the last 35 yr from altimetry satellite missions GEOS3, SEASAT, GEOSAT, ERS-1, ERS-2, GFO, TOPEX/Poseidon, Jason-1, Envisat, Jason-2, CryoSat-2 and recently HY-2A. Over 1750 tide gauge stations located worldwide measure relative sea level providing long time series (totaling longer than 120 yr). Therefore, analysis of tide gauge measurements with the purpose of long-term sea level change research requires a well-defined reference frame. Such reference frame can be realized through precise positions and velocities of Global Positioning System (GPS) stations located at or near tide gauges. One of the purposes of the GPS Tide Gauge Benchmark Monitoring (TIGA) Working Group, former Pilot Project (http://adsc.gfz-potsdam.de/tiga/index_TIGA.html) (Schöne et al., 2009) of the International Global Navigation Satellite System (GNSS) Service (IGS, (Dow et al., 2009)), is to create such a reference frame. The accuracies required by the oceanographic community for sea level studies are about 5–10 mm for station positions and less than 1 mm yr^{-1} for vertical motions (Schöne et al., 2009). Solutions of positions of GPS stations located near to tide gauges were derived by different research groups in 2002–2006 (e.g. Zhang et al., 2008) using relative models for antenna phase centre variations (PCV) and obsolete processing models. However, the switch within the IGS from using a relative to an absolute PCV model mainly affecting the station height, use of new processing software, models and strategies, inclusion of new TIGA GPS stations in the solutions required and made possible a reprocessing within the TIGA project. Within this reprocessing three TIGA analysis centres (a consortium of University of Canberra, University of Tasmania and Australian National University (CTA); German Research Centre for Geosciences (GFZ) and Université de La Rochelle (ULR)) computed global station network solutions. The GFZ and ULR TIGA analysis centres also contributed to the first IGS data reprocessing campaign (IGS repro1, http://acc.igs.org/reprocess.html) and ITRF2008 (Altamimi et al., 2011).

Various authors used GPS measurements to investigate crustal motions at tide gauges and sea level changes regionally (e.g. Buble et al., 2010; Sanchez and Bosch, 2009) and globally (e.g. Wöppelmann et al., 2007, 2009). Recently, several studies have been made to investigate the influence of various types of systematic errors on station position and vertical velocity estimates. Thus, Munekane and Boehm (2010) investigated troposphere-induced errors in GPS-derived geodetic time series. King and Watson (2010) showed the influence of multipath and geometry effects on long GPS coordinate time series. Effects of azimuthal multipath asymmetry on long GPS coordinate time series were studied by Goebell and King (2011). King et al. (2012) examined the simulated effect of the electromagnetic coupling of a GPS antenna-monument on GPS coordinate time series longer than 2.5 yr. Fu et al. (2012) have found 0.3 mm coordinate differences between solutions using ocean tidal loading (OTL) computed using two different centres of mass: the centre of mass of the Earth system and the centre of mass of the solid Earth. The influence of non-tidal ocean loading effects on geodetic GPS heights has been studied by Williams and Penna (2011). The quality assessment of the recently reprocessed GPS realization of the terrestrial reference frame (Collilieux et al., 2011) shows that the GPS-derived origin is at the centimeter level consistent with the Satellite Laser Ranging (SLR) one with a drift lower than 1 mm yr^{-1}. From the recently reprocessed ULR solution, Bouin and Wöppelmann (2010) found agreement within 2 mm yr^{-1} of the tide gauge measurements and vertical velocities for 84 % of the GPS stations co-located with the tide gauges by analyzing 10 yr of continuous GPS data of more than 200 permanent GPS stations distributed worldwide. Global sea-level rise estimates calculated from tide gauge records corrected using GPS data depend on the terrestrial reference frame used. Thus, errors in the reference frame scale rate and origin rate influence the estimated global sea level rise (Collilieux and Wöppelmann, 2011). That is why generation of a stable reference frame containing precise positions of GPS stations located near to tide gauges is very important.

In this paper, we describe the procedure, models used and the results obtained from the analysis of continuous GPS data from a global network of 403 GPS stations for about a 10-yr time span (1998–2007). Vertical velocities of 266 GPS stations with time series longer than 2.5 yr are computed. We compare our solution with the estimates from co-located tide gauges as well as with the GPS-derived vertical velocities from GFZ previous and external solutions.

The remainder of the paper is organized in the following way. The GPS data processing algorithm and the input data, reference frames and models used are described in Sect. 2. The main results of GPS data reprocessing are presented in Sect. 3. The methodology of station vertical velocity computation and some typical and interesting examples of station height changes are given in Sect. 4. Finally, the results obtained are discussed (Sect. 5), conclusions drawn and outlook provided.

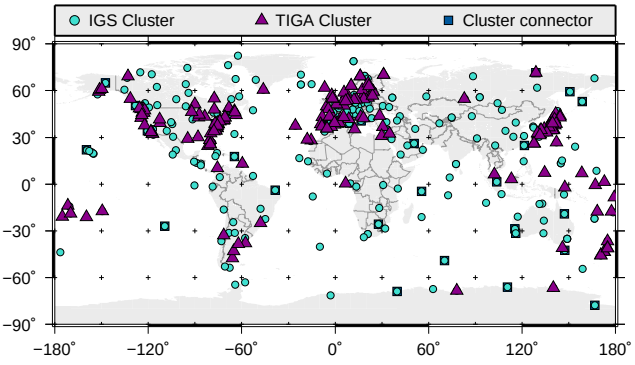

Fig. 1. Global distribution of TIGA and IGS tracking stations used for reprocessing.

2 GPS data processing algorithm

GPS data of a global network of 403 stations covering time span 4 January 1998 to 29 December 2007 (GPS weeks 939 to 1459) were analysed using EPOS-Potsdam software (Gendt et al. (1994), version 7) recently elaborated. The global network of GPS stations (Fig. 1) used for reprocessing was split in two subnetworks. The first subnetwork includes 216 IGS stations; the second subnetwork includes 187 continuous GPS at tide gauges (TIGA) stations: 107 TIGA observing stations and some other new stations. The subnetworks are combined to form daily solutions using up to 30 distributed worldwide IGS reference stations (cluster connectors) using the procedure described in Zhang et al. (2007) and taking into account the global distribution of the reference stations. All available reference stations were used that were available over the time span. The IGS station subnetwork was used to estimate GPS satellite orbits and clocks that were introduced as fixed values when processing GPS data of the TIGA station subnetwork. To stabilize the GPS satellite orbits, daily solutions are combined into three-day solutions by applying orbit continuity constraints (Beutler et al., 1996). Three-day solutions are combined into weekly solutions using the algorithm outlined in Zhang et al. (2007).

The observation data, reference frames, measurement and orbit models used are described in Table 1. The terrestrial reference frame was defined in the following way. The IGS05 (being an IGS realization of ITRF2005 (Altamimi et al., 2007) for GPS stations) was used as a priori terrestrial reference frame. The initial coordinates of stations present in the IGS05 were taken from the IGS05 and estimated for remaining stations. Coordinates of the reference stations were estimated with tight constraints to their initial values, and loose constraints were used for all other stations. The initial values of station velocities were used from the IGS05, if available,

Table 1. Input data, reference frames and models used for GPS data processing.

Item	Description
Observation data	
Basic observable	ionosphere-free linear combination, undifferenced carrier phases and pseudo-ranges
Sampling rate	5 min
Elevation cut-off angle	7°
Elevation-dependent weighting	$1/2\sin(e)$ for $e < 30°$, 1 for $e \geq 30°$
Measurement models	
Satellite antenna to centre of mass offsets	spacecraft-specific z-offsets and block-specific x- and y-offsets from file igs05.atx (Schmid et al., 2007)
Phase centre variations (PCV)	absolute model
PCV for receiver and satellite	file igs05.atx (Schmid et al., 2007)
Antenna radome calibrations	applied, if given in file igs05.atx (Schmid et al., 2007); otherwise the radome effect is neglected and instead standard antenna model (radome => NONE) is used
GPS satellite attitude model	GPS satellite yaw attitude model (Bar-Sever, 1996) based on nominal yaw rates
RHC phase rotation correction	phase wind-up applied (Wu et al., 1993)
Marker to antenna eccentricity	dN, dE, dU eccentricities from site logs applied
Troposphere modelling	empirical Global Pressure and Temperature (GPT) model (Boehm et al., 2007), Saastamoinen "dry" and "wet" model for zenith delay, Global Mapping Function (GMF) (Boehm et al., 2006)
Ionosphere	first-order effect
Tidal corrections	solid Earth tide, permanent tide: applied in tide model, solid Earth pole tide, ocean tide loading (FES2004 model) (McCarthy et al., 2003) ocean tide geocenter: coefficients corrected for centre of mass motion of whole Earth
Non-tidal loadings	atmospheric pressure, ocean bottom pressure, surface hydrology – all not applied
Earth orientation variations	ocean tidal: diurnal and semidiurnal variations in x-, y-pole coordinates and UT1 applied according to McCarthy et al. (2003)
Reference frames	
Inertial reference frame	geocentric, mean equator and equinox of January 1.5, 2000 (J2000.0)
Terrestrial reference frame	IGS05/ITRF2005 (Altamimi et al., 2007) as a priori one
Reference frame interconnection	IAU2000A precession-nutation model, sub-daily nutation with periods less than two days (McCarthy et al., 2003)
Earth orientation parameters	IERS EOP 05 C04 as initial ones, solved polar motion x, y and length of day (LOD)
Orbit models	
Geopotential model	EIGEN-GL04S1 (up to $n = m = 12$) with temporal variations of C_{20}, C_{30}, C_{40}
Tidal variations in geopotential	solid Earth tides, ocean tides, solid Earth pole tide (McCarthy et al., 2003)
Third-body attraction	Sun, Moon, Mercury, Venus, Mars, Jupiter, Saturn, Uranus, Neptune, Pluto (point masses), JPL Planetary Ephemeris DE405
Solar radiation pressure	a priori GPSM-XYZ.1 model, Earth shadow model: penumbra, Moon shadow model,
Relativistic effects	Schwarzschild and Lense–Thirring dynamical correction, gravitational time delay (McCarthy et al., 2003)
Numerical integration of orbit	single step Everhart integrator, direct integration of second-order equations with variable, automatically controlled integration step, arc length: 24 h
Numerical integration of variation equations	multi-step Stoermer–Cowell integrator with direct integration of second-order equations with fixed integration step using Cowell–Kulikov starter procedure, arc length: 24 h

and computed using the NNR-NUVEL1A model (McCarthy et al., 2003) for the remaining stations.

GPS data from up to 300 stations per week were processed using the data processing strategy for huge GNSS global networks (Ge et al., 2006). The following parameters are estimated in the least-square adjustment. The Cartesian station coordinates are estimated weekly using free network strategy with constraints 1–1000 m to a priori values; no station is fixed. Receiver and satellite clocks are solved for at each epoch assuming white noise process. One receiver

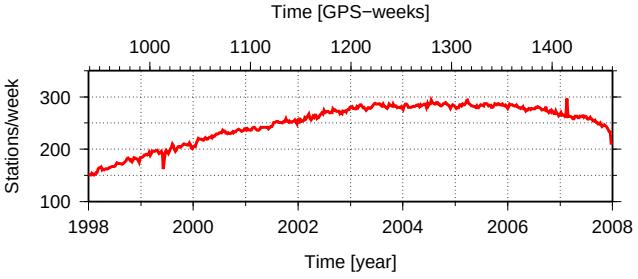

Fig. 2. Number of GPS stations included in the weekly GT1 solutions.

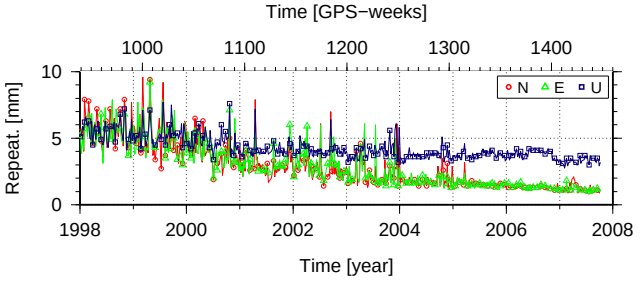

Fig. 3. Weekly overall mean of station coordinate repeatabilities for north (N), east (E) and up (U) components.

clock is fixed and used as a time reference. Satellite initial position and velocity, solar radiation pressure scale, y-bias, sine/cosine terms and stochastic impulses (at noon) are estimated for all satellites once per arc. Yaw rate is adjusted for BLOCK II/IIA satellites during shadow crossing. Troposphere zenith delay coefficients are solved for each station at 1 h intervals. Troposphere gradients in elevation and azimuth are estimated every 12 h for each station. Ambiguities are fixed according to Ge et al. (2005). The Earth rotation parameters (ERPs), namely, x and y Earth pole coordinates and their rates and length of day (LOD), are adjusted daily. In a resulting weekly solution, Universal Time UT1 is fixed for the first day of the week and the daily estimates for UT1 and LOD are constrained to obtain a continuous Earth rotation throughout the week.

3 Results of GPS data reprocessing

The GFZ TIGA GT1 solution contains weekly coordinates of GPS stations, daily values of x and y Earth pole coordinates and their rates and LOD. The solution is available in the Solution (Software/technique) Independent Exchange (SINEX) format via anonymous FTP at TIGA archive (ftp://ftp.gfz-potsdam.de/pub/transfer/kg_igs/igstiga/solutions/) as files /wWWWW/gftWWWW7.snx.Z and at the Crustal Dynamics Data Information System (CDDIS) (ftp://cddis.gsfc.nasa.gov/gps/products/WWWW/repro1/) as files gt1WWWW7.snx.Z, where WWWW stands for GPS week in the range from 0939 till 1459.

We have up to 300 stations included in the weekly solutions (Fig. 2) for the time interval we considered in this study. This figure also illustrates the rapidly growing observation network in the first years.

As an indicator of relative solution stability, the coordinate repeatabilities of daily solutions with respect to the weekly solution were calculated. The averaged values per week over all stations are depicted in Fig. 3. It is clearly visible that the north and east coordinate components improve over the entire time span and reach even 1 mm level. The up component looks relatively stable from 2001 onwards and reaches

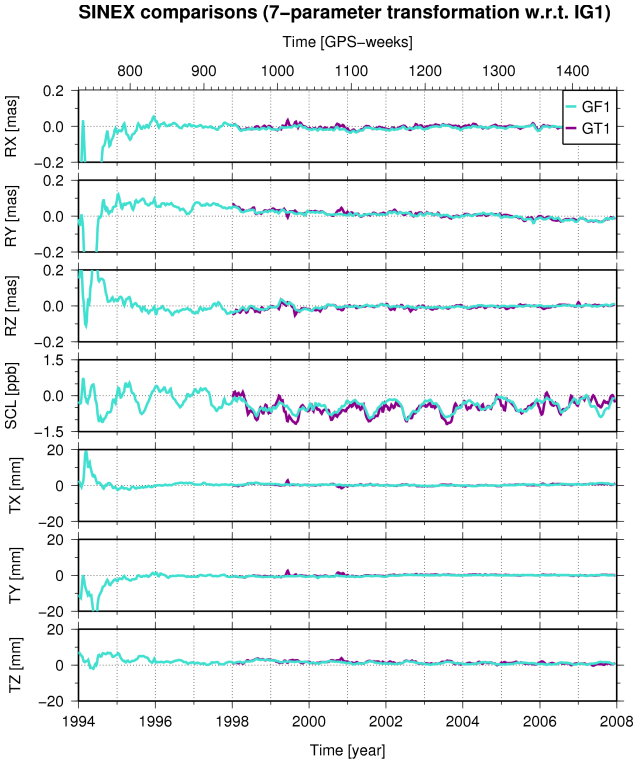

Fig. 4. The time series of weekly Helmert transformation parameters (RX-, RY-, RZ-rotations, TX-, TY-, TZ-translations and scale SCL) of the GT1 and GF1 solutions with respect to the IG1 solution.

3 mm level in 2007. These effects can be also related to the enhancements in the station equipment used.

To assess our weekly coordinate solutions, 7-parameter transformations of GT1 solution and GFZ IGS GF1 solution containing only IGS stations were done with respect to the combined IG1 solution of the IGS repro1 campaign available at ftp://cddis.gsfc.nasa.gov/gps/products/repro1/. The time series of weekly Helmert transformation parameters (X-, Y-, Z-rotations, X-, Y-, Z-translations and scale) of the GT1 solution with respect to the IG1 solution are shown in Fig. 4. The average values and standard deviations of the transformation parameters are -0.004 ± 0.041, 0.007 ± 0.042 and $-0.007 \pm$

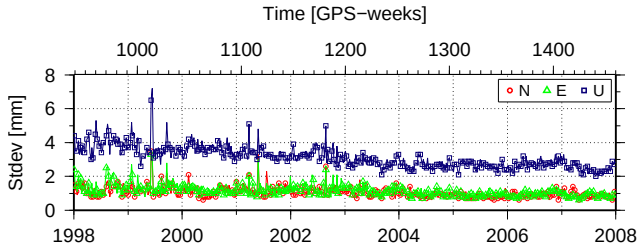

Fig. 5. Standard deviations of the north (N), east (E) and up (U) residual weighted average of the GT1 solution with respect to those of the IG1 combined solution of the IGS repro1 campaign.

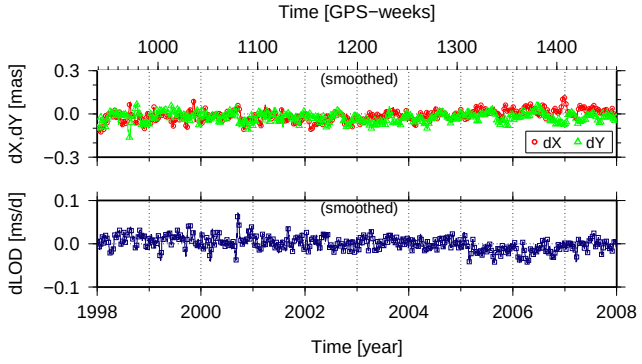

Fig. 6. Comparison of the Earth rotation parameters (X, Y pole coordinates and LOD) of the GT1 solution with respect to those of the IG1 combined solution of the IGS repro1 campaign. The plotted values are smoothed with a sliding 3-day mean.

0.045 mas for X-, Y-, Z-rotations, 0.298 ± 1.074, -0.045 ± 1.069 and 1.403 ± 1.056 mm for X-, Y-, Z-translations and -0.501 ± 0.166 ppb for scale indicating a good agreement of the GT1 solution with the IG1 solution for the common stations. The standard deviations of the GT1 solution residual weighted average with respect to those of the IG1 solution are plotted in Fig. 5. The accuracy of weekly north and east components is about 1 mm for the investigated time span, and the accuracy of the up component reaches 3 mm level at the end of the time interval. Based on these results it can be stated that the required position accuracy needed for the determination of accurate station height time series is fulfilled and that a precise reference frame was obtained.

The daily adjusted values of x and y Earth pole coordinates and length of day of the GT1 solution are compared to those of the IG1 combined solution. The good agreement between the two solutions in x and y pole coordinates with mean values computed using original daily values and standard deviation (scatter in time series of the ERP differences) of -0.012 ± 0.056 and -0.026 ± 0.049 mas and LOD with 0.000 ± 0.023 ms d^{-1} can be seen in Fig. 6.

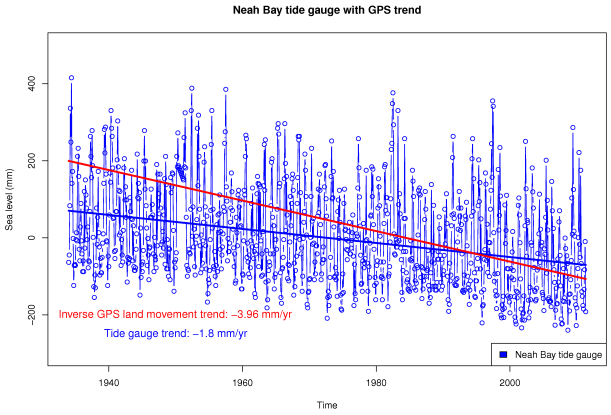

Fig. 7. Height time series and trend for Neah Bay tide gauge and inverse height trend of the co-located GPS station NEAH.

4 Station height changes

4.1 Station vertical velocity computation methodology

Vertical trends were determined from the GT1 SINEX files by extracting Cartesian station coordinates and converting them to longitude, latitude and height using the WGS84 geoid model. The time series were then fitted to extract a linear trend using the standard deviation values as reciprocal weights to account for measurement errors. Trend changes were determined using the Breaks For Additive Seasonal and Trend (BFAST) package (Verbesselt et al., 2010). The BFAST algorithm uses a four-step iterative procedure to detect breakpoints in time series. First, the ordinary least squares (OLS) residuals-based moving sum (MOSUM) test is used to detect whether breakpoints do occur in the time series. If the test indicates a significant change (at the significance level $p < 0.05$), the breakpoints are estimated from the seasonally adjusted data. In the second step, the trend is estimated using robust regression. The OLS-MOSUM test is then applied again in the third step to test for breakpoints in the seasonal component of the time series. In the final step, the seasonal component is estimated from the detrended data. The above steps are iterated until the number and position of breakpoints are unchanged. Details regarding the procedure are described in Verbesselt et al. (2010). The number of breakpoints was adjusted so as to obtain reasonable estimates of the trend changes mirroring the assumed underlying processes.

Antenna changes and other events influencing the vertical trend component were taken from the GPS log files for the respective stations. Some of the GPS stations examined here are located near tide gauges. Here, the trends from the tide gauges were compared with the GPS station height trends and sea level radar altimetry data from the TOPEX/Poseidon mission to separate the origin of the land movement trend

signal where possible. All tide gauge data were retrieved from the Permanent Service for Mean Sea Level (PSMSL) (Woodworth and Player, 2003). Linear trends at tide gauges were determined using a standard linear model with ordinary least square adjustment. TOPEX/Poseidon sea level anomaly data were provided by Saskia Esselborn, GFZ. A seasonal component was extracted using the Loess algorithm from the STL package (Cleveland et al., 1990).

No atmospheric loading corrections were applied to the GPS data, except for BRAZ station, where the hydrological seasonal cycle was the main point of interest, and VAAS and MAR6 stations, for which also hydrological issues were reviewed. That is why the data of BRAZ, VAAS and MAR6 stations were corrected for the atmospheric loading using Green's functions as described in detail in Sect. 4.3.4.

While most stations show consistent, steady height trends, a minority demonstrate deviations caused by antenna or receiver changes. Following the recommendations by Blewitt and Lavallée (2002), stations with the total length of time series shorter than 2.5 yr were not considered for the trend estimation. The vertical velocities of GPS stations located at tide gauges and some IGS stations computed by us are presented in Table 2. The seasonal component was removed from the time series before estimating the trend leading to small error estimates given in Tables 2–3 for our solution.

The time series of height changes of all GPS stations of GT1 solution are available at ftp://ftp.gfz-potsdam.de/pub/home/ig/nana/GPS_station_heights/. In the following, a few interesting examples are treated in detail.

4.2 Stations with prominent secular height trend

4.2.1 Plate tectonics: Neah Bay (NEAH), Canada

Neah Bay, Washington, lies on the Juan de Fuca Strait in the Cascadia subduction zone, which is subject to crustal uplift as the North American plate is shifted over the Juan de Fuca plate. The GPS time series provides a secular trend of $3.96 \pm 0.02\,\mathrm{mm\,yr^{-1}}$ ($4.0 \pm 0.0\,\mathrm{mm\,yr^{-1}}$ with a seasonal signal removed), and the tide gauge measurements give a secular trend of $-1.8 \pm 0.1\,\mathrm{mm\,yr^{-1}}$ (Fig. 7). This agrees well with the results of Verdonck (2006), who computed an estimated rate of land movement of $4.0 \pm 0.1\,\mathrm{mm\,yr^{-1}}$. In his estimate, he subtracts a mean eustatic sea level rise $2.0\,\mathrm{mm\,yr^{-1}}$ from the trend calculated from the tide gauge data ($-2.0\,\mathrm{mm\,yr^{-1}}$).

4.2.2 Glacial isostatic adjustment: Fennoscandia (Skellefteå, Sweden (Furuogrund tide gauge), Mårtsbo, Sweden (Nedre Gavle tide gauge), and Vaasa, Finland (Vaasa tide gauge))

These three stations, all located around the Gulf of Bothnia, are subject to land movement processes due to glacial isostatic adjustment (GIA). All stations show large secular uplift rates with Skellefteå leading at $10.80 \pm 0.06\,\mathrm{mm\,yr^{-1}}$, followed by Vaasa at $8.66 \pm 0.04\,\mathrm{mm\,yr^{-1}}$ and Mårtsbo ($7.62 \pm 0.01\,\mathrm{mm\,yr^{-1}}$).

The GPS station Skellefteå lies in the vicinity of Furuogrund tide gauge (approximately 11 km distance). The tide gauge trend computed by us using full data and for the case, when the annual signal is removed, is $-8.1 \pm 0.2\,\mathrm{mm\,yr^{-1}}$. So, the residual sea level rise from the sum of the tide gauge and vertical land movement trends is $2.7 \pm 0.3\,\mathrm{mm\,yr^{-1}}$.

Nedre Gavle tide gauge situated at approximately 10 km distance from the GPS station MAR6 has a trend of $-6.0 \pm 0.2\,\mathrm{mm\,yr^{-1}}$ (1896–1986) computed by us (Fig. 8, upper panel). Since the gauge stopped operating in 1986, there is no common period with the GPS station. The comparison with the land movement trend at Mårtsbo ($7.62 \pm 0.01\,\mathrm{mm\,yr^{-1}}$) indicates that a large part of the tide gauge signal can be explained by the land movement through GIA. Assuming that the GIA trend was constant over the last 100 yr, the residual sea level trend from the sum of the tide gauge relative sea level trend and land movement signals is $1.62 \pm 0.2\,\mathrm{mm\,yr^{-1}}$.

Vaasa tide gauge trend estimated by us is $-7.6 \pm 0.2\,\mathrm{mm\,yr^{-1}}$. The vertical land motion at the co-located GPS station VAAS with atmospheric loading correction applied is $8.6 \pm 0.2\,\mathrm{mm\,yr^{-1}}$. So, the sum of the tide gauge trend and vertical land motion leads to the absolute sea level rise at Vaasa equal to $1.0 \pm 0.2\,\mathrm{mm\,yr^{-1}}$.

Despite rather large distance (>340 km) between GPS stations Vaasa and Mårtsbo, the height time series for these stations are strongly correlated at $R^2 = 0.93$. When reduced for atmospheric loading, the correlation drops only marginally to $R^2 = 0.92$ (Fig. 8, lower panel). A large part of this is due to the trend. However, even the detrended time series score a $R^2 = 0.45$ correlation (Fig. 9, lower panel). The deviations between the two series consist mainly in an annual multi-week drift at Vaasa, which is caused by snow cover on the antenna. This figure demonstrates that the drift signals coincide with the periods of increased snow coverage in the area. The snow cover data were taken from Robert Dill's hydrological land surface discharge model (LSDM, Dill (2008)). Its influence on the correlation is checked by decomposing the detrended time series and determining the correlations for the respective components. When the linear trend is removed, the time series correlate at $R^2 = 0.73$ for the residual nonlinear trend, and $R^2 = 0.59$ for the full series with the nonlinear trend removed. Only the snow-dominated seasonal cycle shows no correlation at $R^2 = -0.09$. It is worth to remark that the snow disturbance is correctly removed by the STL algorithm when removing the seasonal cycle. This example illustrates that hydrological errors occurring at a seasonal frequency can be easily and automatically removed when the seasonal cycle is calculated by taking the multi-year monthly mean, instead of fitting a sine. The tide gauge time series exhibit the same strong correlation, with $R^2 = 0.95$ for the full time series and $R^2 = 0.91$ for the detrended time series, in

Table 2. Linear height trends at GPS stations. The table contains all stations from the TIGA reprocessing campaign with time series longer than 2.5 yr from which a reasonable linear trend could be determined. Time series that showed large gaps were left out, as were stations with obvious jumps or trend changes. Some of these examples are treated in Sect. 4. A seasonal trend was removed for all stations. Atmospheric corrections were not applied. The station longitude and latitude are expressed in degrees, arc minutes and arc seconds. The beginning and the end of the time series are given as the GPS week number. The length of the time series is provided in years.

Station	Name	Longitude	Latitude	Trend (mm yr^{-1})	Begin	End	Length
0194	Tobishima, Sakata, Japan	139 32 51.6	39 11 08.0	0.90 ± 0.03	939	1459	10.0
ABER	Aberdeen, UK	357 55 11.2	57 08 38.4	1.69 ± 0.02	976	1459	9.3
AJAC	Ajaccio, France	8 45 45.4	41 55 38.8	0.31 ± 0.02	1045	1446	7.7
ALAC	Alicante, Spain	359 31 07.6	38 20 20.1	0.23 ± 0.01	1021	1459	8.4
ALGO	Algonquin Park, Canada	281 55 43.1	45 57 20.9	3.47 ± 0.02	939	1459	10.0
ALIC	Alice Springs, Australia	133 53 07.9	–23 40 12.4	0.38 ± 0.03	939	1459	10.0
ALME	Almeria, Spain	357 32 26.0	36 51 09.1	1.40 ± 0.03	1094	1459	7.0
ALRT	Alert, Canada	297 39 34.3	82 29 39.5	5.15 ± 0.03	1175	1459	5.5
ANDE	Andenes, Norway	16 08 05.3	69 19 33.8	2.48 ± 0.04	1096	1424	6.3
ANDO	Andenes, Norway	16 00 30.6	69 16 41.9	2.49 ± 0.03	939	1424	9.3
ANKR	Ankara, Turkey	32 45 30.5	39 53 14.5	-0.73 ± 0.05	939	1455	9.9
ANTA	Antalya, Turkey	30 36 33.9	36 49 42.6	-2.27 ± 0.18	1245	1455	4.0
AOML	Key Biscayne, FL, USA	279 50 16.1	25 44 04.9	0.50 ± 0.03	939	1265	6.3
AREQ	Arequipa, Peru	288 30 25.9	–16 27 55.9	3.81 ± 0.02	1138	1459	6.2
ARTU	Arti Ekaterinburg, Russia	58 33 37.6	56 25 47.4	0.90 ± 0.04	1021	1459	8.4
AUCK	Whangaparaoa No3, NZ	174 50 03.8	–36 36 10.2	-1.55 ± 0.04	939	1459	10.0
BAHR	Manama, Bahrain	50 36 29.3	26 12 32.9	0.53 ± 0.02	939	1459	10.0
BAIE	Baie Comeau, Canada	291 44 12.0	49 11 12.6	3.49 ± 0.03	1147	1459	6.0
BAKE	Baker Lake, Canada	263 59 51.6	64 19 04.2	10.82 ± 0.04	1147	1438	5.6
BILI	Bilibino, Russia	166 26 16.7	68 04 34.1	0.28 ± 0.03	1025	1459	8.3
BISH	Bishkek, Kyrgyzstan	74 35 39.1	42 52 32.1	-1.42 ± 0.05	939	1359	8.1
BJFS	Beijing, Fangshan, China	115 53 32.9	39 36 31.0	3.47 ± 0.05	1032	1459	8.2
BOGT	Bogotá, Colombia	285 55 08.6	4 38 24.3	-44.21 ± 0.19	942	1459	9.9
BOR1	Borowice, Poland	17 04 24.4	52 16 37.0	-0.04 ± 0.01	1192	1459	5.1
BRAZ	Brasilia, Brazil	312 07 19.7	–15 56 50.9	-0.18 ± 0.05	940	1459	10.0
BRMU	Bermuda, UK	295 18 13.4	32 22 13.4	-0.54 ± 0.03	939	1459	10.0
BRUS	Brussels, Belgium	4 21 33.2	50 47 52.1	0.78 ± 0.03	939	1459	10.0
BUR1	Burnie, Tasmania	145 54 53.4	–41 03 00.2	-0.24 ± 0.03	1004	1412	7.8
CABL	Port Orford, OR, USA	235 26 12.0	42 50 10.0	-0.06 ± 0.04	1188	1459	5.2
CAGL	Cagliari, Italy	8 58 21.9	39 08 09.3	-0.15 ± 0.03	939	1459	10.0
CANT	Santander, Spain	356 12 07.0	43 28 19.1	0.38 ± 0.04	1094	1459	7.0
CART	Cartagena, Colombia	284 27 58.1	10 23 28.8	-2.12 ± 0.07	1047	1456	7.9
CAS1	Casey, Antarctica	110 31 10.9	–66 17 00.1	-0.41 ± 0.08	1088	1453	7.0
CASC	Cascais, Portugal	350 34 53.3	38 41 36.3	0.19 ± 0.03	955	1459	9.7
CCV3	Cape Canaveral, FL, USA	279 27 17.2	28 27 36.8	0.23 ± 0.22	969	1411	8.5
CEDU	Ceduna, Australia	133 48 35.4	–31 52 00.0	-1.07 ± 0.03	944	1459	9.9
CFAG	Caucete, Argentina	291 46 02.5	–31 36 07.8	-0.69 ± 0.04	939	1459	10.0
CHA1	Charleston, SC, USA	280 09 25.7	32 45 27.2	-0.73 ± 0.04	988	1245	4.9
CHAT	Chatham Island, NZ	183 26 03.0	–43 57 20.8	-0.37 ± 0.02	939	1459	10.0
CHUM	Chumysh, Kazakhstan	74 45 03.9	42 59 54.6	0.40 ± 0.02	939	1459	10.0
CHUR	Churchill, Canada	265 54 40.6	58 45 32.7	9.67 ± 0.03	939	1459	10.0
CKIS	Rarotonga, Cook Islands, NZ	200 11 57.8	–21 12 03.7	0.04 ± 0.03	1131	1459	6.3
COCO	Cocos Island, Australia	96 50 02.3	–12 11 18.0	-0.68 ± 0.04	939	1459	10.0
CONZ	Concepcion, Chile	286 58 28.3	–36 50 37.5	0.39 ± 0.11	1170	1459	5.6
CRO1	St. Croix, U.S. Virgin Isl.	295 24 56.4	17 45 24.8	-1.87 ± 0.03	939	1459	10.0
CSAR	Caesarea, Israel	34 53 24.7	32 29 17.7	0.50 ± 0.04	1263	1459	3.8
DAEJ	Daejeon, South Korea	127 22 28.1	36 23 57.9	1.51 ± 0.07	1001	1459	8.8
DARW	Darwin, Australia	131 07 57.9	–12 50 37.3	-0.17 ± 0.07	1242	1457	4.1
DAV1	Davis, Antarctica	77 58 21.4	–68 34 38.4	-1.92 ± 0.03	1038	1459	8.1
DRAG	Metzoke Dragot, Israel	35 23 31.4	31 35 35.5	3.15 ± 0.03	1033	1459	8.2
DRAO	Penticton, Canada	240 22 30.1	49 19 21.4	-0.56 ± 0.03	1188	1459	5.2
DUBO	Lac du Bonnet, Canada	264 08 01.7	50 15 31.7	2.13 ± 0.06	1288	1459	3.3
DUM1	Dumont d'Urville, Antarctica	140 00 07.0	–66 39 54.3	-2.11 ± 0.02	939	1459	10.0
DUNT	Dunedin, NZ	170 37 45.9	–45 48 51.5	-1.63 ± 0.02	1029	1459	8.3
EIJS	Eijsden, Netherlands	5 41 01.0	50 45 29.7	3.58 ± 0.06	939	1459	10.0
ESTI	Esteli, Nicaragua	273 38 16.3	13 05 58.3	5.06 ± 0.06	1061	1207	2.8
FAIR	Fairbanks, AK, USA	212 30 02.7	64 58 40.8	2.52 ± 0.06	1188	1459	5.2

Table 2. Continued.

Station	Name	Longitude	Latitude	Trend (mm yr^{-1})	Begin	End	Length
FLIN	Flin Flon, Canada	258 01 19.1	54 43 32.1	3.53 ± 0.03	1288	1459	3.3
FORT	Fortaleza, Brazil	321 34 27.8	–3 52 38.8	1.40 ± 0.06	1188	1370	3.5
FREE	Freeport, Bahamas	281 00 26.8	26 42 09.1	1.78 ± 0.07	1013	1137	2.4
FTS1	Fort Stevens, OR, USA	236 02 38.1	46 12 17.6	2.82 ± 0.02	939	1459	10.0
GAL1	Galveston, TX, USA	265 15 47.5	29 19 47.6	-4.76 ± 0.05	939	1226	5.5
GALA	Galapagos Isl., Ecuador	269 41 47.0	0 44 33.7	-2.59 ± 0.09	939	1192	4.9
GENO	Genova, Italy	8 55 16.1	44 25 09.8	-0.48 ± 0.04	967	1459	9.5
GETI	Geting, Malaysia	102 06 19.7	6 13 34.3	3.39 ± 0.02	990	1186	3.8
GLPT	Gloucester Point, VA, USA	283 30 02.0	37 14 54.8	-2.61 ± 0.03	939	1385	8.6
GLSV	Kiev, Ukraine	30 29 48.2	50 21 51.1	0.20 ± 0.03	949	1459	9.8
GODE	Greenbelt, MD, USA	283 10 23.4	39 01 18.2	-1.56 ± 0.03	939	1459	10.0
GOLD	Goldstone, CA, USA	243 06 38.7	35 25 30.6	0.25 ± 0.09	1088	1459	7.1
GOPE	Ondrejov, Czech Republic	14 47 08.2	49 54 49.3	-1.44 ± 0.04	1192	1459	5.1
GRAS	Grasse, France	6 55 14.1	43 45 17.1	0.59 ± 0.01	939	1459	10.0
GRAZ	Graz, Austria	15 29 36.5	47 04 01.7	0.43 ± 0.02	939	1459	10.0
GUAM	Dededo, Guam	144 52 06.1	13 35 21.6	-0.01 ± 0.04	1138	1459	6.2
GUAT	Guatemala, Guatemala	269 28 47.3	14 35 25.5	1.04 ± 0.06	1072	1459	7.4
HELG	Helgoland Island, Germany	7 53 35.1	54 10 28.1	1.04 ± 0.02	1035	1459	8.2
HILO	Hilo, Hawaii, USA	204 56 50.3	19 43 09.1	-1.66 ± 0.02	939	1454	9.9
HLFX	Halifax, Canada	296 23 19.4	44 41 00.8	-1.13 ± 0.02	1147	1459	6.0
HNLC	Honolulu, Hawaii, USA	202 08 07.6	21 18 11.8	-0.66 ± 0.04	939	1459	10.0
HNPT	Horn Point, Cambridge, MD, USA	283 52 10.7	38 35 19.7	-2.51 ± 0.02	1038	1459	8.1
HOB2	Hobart, Australia	147 26 19.4	–42 48 17.0	-0.53 ± 0.04	1038	1459	8.1
HOFN	Hoefn, Iceland	344 48 07.5	64 16 02.3	13.52 ± 0.06	1138	1459	6.2
HOLM	Holman, Canada	242 14 19.5	70 44 10.7	2.63 ± 0.03	1129	1459	6.3
HRAO	Hartebeesthoek, South Africa	27 41 13.1	–25 53 24.4	-0.72 ± 0.02	942	1457	9.9
IISC	Bangalore, India	77 34 13.3	13 01 16.2	0.06 ± 0.03	939	1459	10.0
INEG[1]	Aguascalientes, Mexico	257 42 56.9	21 51 22.2	-87.66 ± 0.28	1038	1158	2.3
IRKT	Irkutsk, Russia	104 18 58.5	52 13 08.5	1.26 ± 0.03	939	1459	10.0
JOZE	Jozefoslaw, Poland	21 01 53.5	52 05 50.2	1.00 ± 0.01	939	1459	10.0
JPLM	Pasadena, CA, USA	241 49 36.4	34 12 17.4	0.91 ± 0.06	939	1459	10.0
KARR	Karratha, Australia	117 05 49.9	–20 58 53.1	0.55 ± 0.04	939	1459	10.0
KELS	Kelso, WA, USA	237 06 14.2	46 07 05.4	-0.53 ± 0.02	939	1444	9.7
KEN1	Kenai, AK, USA	208 38 59.3	60 40 30.3	9.17 ± 0.12	939	1443	9.7
KERG	Kerguelen, Kerguelen Islands	70 15 19.9	–49 21 05.3	0.99 ± 0.02	1188	1459	5.2
KGN0	Koganei, Japan	139 29 18.7	35 42 24.4	0.83 ± 0.02	1128	1368	4.6
KIRI	Betio, Kiribati	172 55 22.4	1 21 16.5	-2.03 ± 0.06	1177	1459	5.4
KIRU	Kiruna, Sweden	20 58 06.4	67 51 26.5	6.48 ± 0.07	939	1459	10.0
KIT3	Kitab, Uzbekistan	66 53 07.6	39 08 05.2	-0.95 ± 0.05	939	1459	10.0
KODK	Kodiak, AK, USA	207 29 55.0	57 44 06.4	8.82 ± 0.10	1039	1385	6.7
KOSG	Kootwijk, Netherlands	5 48 34.7	52 10 42.3	-0.44 ± 0.02	939	1459	10.0
KOUR	Kourou, French Guyana	307 11 38.5	5 15 07.9	-0.32 ± 0.09	1088	1459	7.1
KSTU	Krasnoyarsk, Russia	92 47 37.8	55 59 35.7	1.13 ± 0.04	949	1289	6.5
KUNM	Kunming, China	102 47 49.9	25 01 46.3	-0.08 ± 0.06	978	1459	9.3
KUUJ	Kuujjuarapik, Canada	282 15 16.4	55 16 42.1	11.52 ± 0.06	1173	1445	5.2
KWJ1	Kwajalein, Marshall Islands	167 43 48.9	8 43 19.9	-1.63 ± 0.14	939	1176	4.6
KYW1	Key West, FL, USA	278 20 49.1	24 34 56.2	-1.01 ± 0.01	939	1448	9.8
LAE1	Lae, Papua New Guinea	146 59 35.5	–6 40 25.3	-5.39 ± 0.04	1095	1384	5.6
LAGO	Lagos, Portugal	351 19 53.8	37 05 56.2	-0.76 ± 0.02	1056	1459	7.8
LAMP	Lampedusa, Italy	12 36 20.4	35 29 59.2	0.42 ± 0.02	1002	1459	8.8
LAUT	Lautoka, Fiji	177 26 47.7	–17 36 31.7	-0.19 ± 0.11	1141	1459	6.1
LHAS	Lhasa, Tibet, China	91 06 14.4	29 39 26.4	0.82 ± 0.03	939	1412	9.1
LPGS	La Plata, Argentina	302 04 03.7	–34 54 24.3	2.78 ± 0.05	939	1459	10.0
LROC	La Rochelle, France	358 46 50.5	46 09 32.2	0.29 ± 0.03	1141	1459	6.1
LYTT	Lyttelton, NZ	172 43 20.0	–43 36 21.0	-0.95 ± 0.02	1037	1459	8.1
MAC1	MacQuarie, Australia	158 56 09.0	–54 29 58.3	-2.84 ± 0.03	939	1459	10.0
MADR	Madrid (Robledo), Spain	355 45 01.2	40 25 45.0	-0.22 ± 0.08	939	1459	10.0
MALI	Malindi, Kenya	40 11 39.8	-2 59 45.3	-0.87 ± 0.11	939	1459	10.0
MAR6	Mårtsbo, Sweden	17 15 30.7	60 35 42.5	7.62 ± 0.01	999	1459	8.8
MARS	Marseille, France	5 21 13.6	43 16 43.6	0.33 ± 0.02	966	1459	9.5

Table 2. Continued.

Station	Name	Longitude	Latitude	Trend (mm yr^{-1})	Begin	End	Length
MAS1	Maspalomas, Canary Islands, Spain	344 22 00.2	27 45 49.5	-0.62 ± 0.04	1038	1459	8.1
MATE	Matera, Italy	16 42 16.0	40 38 56.9	1.05 ± 0.02	939	1459	10.0
MAW1	Mawson, Antarctica	62 52 14.6	–67 36 17.2	-0.95 ± 0.01	939	1459	10.0
MBAR	Mbarara, Uganda	30 44 16.4	0 36 05.3	2.68 ± 0.05	1123	1455	6.4
MDO1	McDonald, TX, USA	255 59 06.0	30 40 49.8	0.27 ± 0.03	939	1459	10.0
METS	Metsahovi, Finland	24 23 43.1	60 13 02.9	4.70 ± 0.01	939	1459	10.0
MIL1	Milwaukee, WI, USA	272 06 41.6	43 00 09.1	-3.40 ± 0.02	939	1401	8.9
MKEA	Mauna Kea, Hawaii, USA	204 32 37.2	19 48 04.9	-2.46 ± 0.03	939	1459	10.0
MOB1	Mobile, AL, USA	271 58 33.2	30 13 39.1	-4.03 ± 0.05	939	1459	10.0
MPLA	Mar del Plata, Argentina	302 28 07.7	–38 02 08.3	-2.26 ± 0.14	1187	1455	5.2
MQZG	McQueens Valley, NZ	172 39 16.9	–43 42 09.8	-2.11 ± 0.04	1029	1459	8.3
NAIN	Nain, Canada	298 18 40.6	56 32 13.1	4.09 ± 0.03	1197	1459	5.0
NANO	Nanoose Bay, Canada	235 54 48.7	49 17 41.3	0.60 ± 0.03	939	1459	10.0
NCDK	Duck, NC, USA	284 14 55.5	36 10 55.4	-3.16 ± 0.15	1267	1417	2.9
NEAH	Neah Bay, WA, USA	235 22 30.3	48 17 52.3	3.96 ± 0.02	939	1459	10.0
NEIA	Cananeia, Brazil	312 04 30.1	–25 01 12.9	0.49 ± 0.01	1172	1458	5.5
NEWL	Newlyn, UK	354 27 26.0	50 06 10.9	-0.17 ± 0.02	977	1458	9.3
NEWP	Newport, OR, USA	235 56 17.2	44 35 06.1	1.57 ± 0.02	947	1418	9.1
NICO	Nicosia, Cyprus	33 23 47.2	35 08 27.6	0.80 ± 0.04	939	1459	10.0
NKLG	N'Koltang, Gabon	9 40 19.6	0 21 14.1	-0.03 ± 0.03	1055	1458	7.8
NOUM	Noumea, New Caledonia	166 24 36.7	–22 16 11.5	-3.06 ± 0.05	939	1419	9.2
NPLD	Teddington, UK	359 39 37.3	51 25 15.5	0.61 ± 0.04	1095	1458	7.0
NRC1	Ottawa, Canada	284 22 34.2	45 27 15.0	3.49 ± 0.01	939	1459	10.0
NRIL	Norilsk, Russia	88 21 35.2	69 21 42.6	2.24 ± 0.04	1079	1459	7.3
NSTG	North Shields, UK	358 33 36.5	55 00 26.7	0.70 ± 0.02	1213	1459	4.7
NVSK	Novosibirsk, Russia	83 14 07.6	54 50 26.2	0.63 ± 0.05	1070	1459	7.5
NYA1	Ny-Alesund, Norway	11 51 55.1	78 55 46.4	8.54 ± 0.04	948	1459	9.8
NYAL	Ny-Alesund, Norway	11 51 54.3	78 55 46.5	8.81 ± 0.04	945	1459	9.9
OBE2	Oberpfaffenhofen 2, Germany	11 16 47.5	48 05 10.2	0.88 ± 0.05	1126	1457	6.4
OBER	Oberpfaffenhofen, Germany	11 16 47.5	48 05 10.2	-0.67 ± 0.10	939	1115	3.4
ONSA	Onsala, Sweden	11 55 31.9	57 23 43.1	1.90 ± 0.05	939	1459	10.0
OUS2	Dunedin, NZ	170 30 39.4	–45 52 10.1	-1.38 ± 0.03	1164	1459	5.7
P102	Okushiri, Japan	139 29 21.1	42 04 43.6	-4.12 ± 0.03	1214	1459	4.7
P103	Asamushi, Aomori, Japan	140 51 33.1	40 53 51.0	1.81 ± 0.01	1212	1459	4.8
P104	Oga, Japan	139 42 12.4	39 56 31.6	3.66 ± 0.02	1221	1459	4.6
P108	Aburatsubo, Miura, Japan	139 36 55.9	35 09 36.6	-1.71 ± 0.02	1212	1459	4.8
P109	Ogi, Japan	138 16 52.5	37 48 53.1	2.46 ± 0.02	1221	1459	4.6
P110	Kashiwazaki, Japan	138 30 30.7	37 21 23.6	-2.17 ± 0.23	1224	1458	4.5
P112	Mikuni, Japan	136 08 55.8	36 15 16.5	-0.95 ± 0.01	1221	1459	4.6
P114	Tago, Nishiizu, Japan	138 45 51.1	34 48 24.8	-2.34 ± 0.01	1222	1459	4.6
P115	Yaizu, Japan	138 19 38.7	34 52 14.4	-2.92 ± 0.06	1222	1459	4.6
P116	Onisaki, Tokoname, Japan	136 49 25.8	34 54 14.3	8.27 ± 0.06	1222	1459	4.6
P117	Kainan, Japan	135 11 29.5	34 08 38.9	4.34 ± 0.01	1222	1459	4.6
P118	Tajiri, Iwami, Japan	134 18 57.4	35 35 37.3	-0.43 ± 0.01	1223	1459	4.5
P119	Susa, Japan	131 36 16.7	34 37 39.3	0.49 ± 0.02	1213	1459	4.7
P120	Kure, Nakatosa, Japan	133 14 36.6	33 20 00.6	7.03 ± 0.07	1222	1459	4.6
P124	Okinawa, Tinen, Japan	127 49 28.8	26 10 46.1	0.15 ± 0.03	1222	1459	4.6
P201	Wakkanai, Japan	141 41 07.2	45 24 28.2	1.51 ± 0.02	1212	1459	4.8
P202	Abashiri, Japan	144 17 08.9	44 01 09.9	1.95 ± 0.02	1221	1459	4.6
P203	Kushiro, Japan	144 22 17.0	42 58 32.1	1.96 ± 0.09	1263	1459	3.8
P204	Hakodate, Japan	140 43 28.3	41 46 54.0	1.29 ± 0.03	1214	1459	4.7
P206	Mera, Tateyama, Japan	139 49 29.7	34 55 07.7	-1.12 ± 0.00	1223	1459	4.5
P209	Hamada, Japan	132 03 58.4	34 53 50.3	-0.67 ± 0.01	1223	1459	4.5
P211	Aburatsu, Nichinan, Japan	131 24 33.5	31 34 37.1	-0.68 ± 0.05	1220	1459	4.6
P212	Naha, Japan	127 39 54.7	26 12 48.0	-0.18 ± 0.01	1222	1459	4.6
P213	Chichijima, Ogasawara, Japan	142 11 40.6	27 05 38.2	0.10 ± 0.08	1215	1459	4.7
PALM	Palmer Station, Antarctica	295 56 56.0	–64 46 30.3	3.91 ± 0.06	965	1446	9.3
PAPE	Papeete, Tahiti	210 25 38.2	–17 31 59.1	-0.12 ± 0.03	1253	1459	4.0
PARC	Punta Arenas, Chile	289 07 12.4	–53 08 13.0	-1.26 ± 0.02	990	1459	9.0
PBL1	Point Blunt, CA, USA	237 34 51.8	37 51 11.0	-0.15 ± 0.07	939	1261	6.2

Table 2. Continued.

Station	Name	Longitude	Latitude	Trend (mm yr^{-1})	Begin	End	Length
PDEL	Ponta Delgada, Azores, Portugal	334 20 14.0	37 44 51.9	-2.08 ± 0.03	1058	1459	7.7
PERT	Perth, Australia	115 53 06.9	–31 48 07.1	-6.30 ± 0.05	939	1459	10.0
PETP	Petropavlovsk-Kamchatsky, Russia	158 36 25.5	53 04 00.2	-4.15 ± 0.07	978	1459	9.3
PGC5	North Saanich, Canada	236 32 55.9	48 38 54.7	-1.36 ± 0.16	1315	1459	2.8
PIMO	Manila, Philippines	121 04 39.8	14 38 08.6	0.80 ± 0.01	1200	1459	5.0
PLO3	Point Loma, CA, USA	242 45 25.1	32 39 55.5	-0.01 ± 0.09	939	1382	8.5
PLUZ	Las Palmas, Canary Islands, Spain	344 35 32.6	28 08 48.2	-1.05 ± 0.06	1265	1438	3.3
PNGM	Lombrum, Papua New Guinea	147 21 57.6	–2 02 35.6	-1.64 ± 0.16	1164	1459	5.7
POHN	Pohnpei, Micronesia	158 12 36.4	6 57 35.8	-1.02 ± 0.05	1216	1459	4.7
POLV	Poltava, Ukraine	34 32 34.5	49 36 09.4	-0.25 ± 0.04	1119	1459	6.5
POR4	New Castle, NH, USA	289 17 25.7	43 04 15.7	0.88 ± 0.10	1056	1295	4.6
POTS	Potsdam, Germany	13 03 57.9	52 22 45.5	-0.63 ± 0.04	939	1459	10.0
PRDS	Calgary, Canada	245 42 23.4	50 52 16.9	0.70 ± 0.08	939	1459	10.0
QAQ1	Qaqortoq, Greenland	313 57 08.1	60 42 55.0	4.97 ± 0.06	1167	1459	5.6
RABT	Rabat, Morocco	353 08 44.6	33 59 53.2	-1.08 ± 0.03	1062	1459	7.6
RAMO	Mitzpe Ramon, Israel	34 45 47.3	30 35 51.4	1.08 ± 0.04	961	1459	9.6
RED1	Reedy Point, DE, USA	284 25 48.1	39 33 41.2	-2.39 ± 0.07	996	1424	8.2
REYK	Reykjavik, Iceland	338 02 40.2	64 08 19.6	-3.08 ± 0.05	939	1459	10.0
REYZ	Reykjavik, Iceland	338 02 40.3	64 08 19.7	-1.09 ± 0.03	1170	1445	5.3
RIGA	Riga, Latvia	24 03 31.6	56 56 55.0	1.56 ± 0.03	999	1459	8.8
RIOG	Rio Grande, Argentina	292 14 56.0	–53 47 07.7	2.99 ± 0.05	939	1416	9.2
RWSN	Rawson, Argentina	294 53 33.9	–43 17 56.0	-0.01 ± 0.02	1046	1456	7.9
SAG1	Saginaw Bay, MI, USA	276 09 44.0	43 37 43.1	-3.04 ± 0.02	939	1454	9.9
SANT	Santiago, Chile	289 19 53.2	–33 09 01.0	3.17 ± 0.03	939	1459	10.0
SCH2	Schefferville, Canada	293 10 02.6	54 49 55.5	10.88 ± 0.03	939	1459	10.0
SCUB	Santiago de Cuba, Cuba	284 14 15.7	20 00 43.4	0.12 ± 0.07	1050	1459	7.9
SEAT	Seattle, WA, USA	237 41 25.9	47 39 14.3	-0.20 ± 0.03	939	1459	10.0
SELD	Seldovia, AK, USA	208 17 36.0	59 26 44.6	10.21 ± 0.08	1085	1459	7.2
SFER	San Fernando, Spain	353 47 39.7	36 27 51.6	1.22 ± 0.03	991	1459	9.0
SHEE	Sheerness, UK	0 44 36.3	51 26 44.5	-0.32 ± 0.05	939	1459	10.0
SIO3	Scripps, CA, USA	242 44 58.5	32 51 52.9	2.54 ± 0.07	1038	1459	8.1
SKE0	Skellefteå, Sweden	21 02 53.8	64 52 45.1	10.80 ± 0.06	1232	1459	4.4
SOFI	Sofia, Bulgaria	23 23 41.0	42 33 21.9	0.17 ± 0.02	939	1459	10.0
SOL1	Solomons Island, MD, USA	283 32 46.0	38 19 08.0	0.19 ± 0.34	939	1437	9.6
STJO	St. John's, Canada	307 19 20.1	47 35 42.9	0.59 ± 0.02	939	1459	10.0
SUTH	Sutherland, South Africa	20 48 37.7	–32 22 48.8	-0.28 ± 0.02	953	1458	9.7
SUWN	Suwon-shi, South Korea	127 03 15.3	37 16 31.9	0.61 ± 0.06	939	1459	10.0
SYOG	Syowa, Antarctica	39 35 01.5	–69 00 25.0	0.64 ± 0.04	939	1459	10.0
TERS	Terschelling, Netherlands	5 13 09.8	53 21 45.9	0.80 ± 0.05	939	1459	10.0
THTI	Tahiti, Tahiti	210 23 36.8	–17 34 37.4	-0.89 ± 0.03	960	1459	9.6
THU3	Thule Air Base, Greenland	291 10 29.9	76 32 13.4	5.05 ± 0.04	1167	1459	5.6
TID1	Tidbinbilla, Australia	148 58 48.0	–35 23 57.1	0.22 ± 0.04	939	1459	10.0
TID2	Tidbinbilla, Australia	148 58 48.0	–35 23 57.1	0.36 ± 0.04	939	1453	9.9
TIDB	Tidbinbilla, Australia	148 58 48.0	–35 23 57.1	-0.93 ± 0.04	1088	1459	7.1
TIXI	Tixi, Russia	128 51 59.1	71 38 04.1	0.89 ± 0.02	978	1459	9.3
TLSE	Toulouse, France	1 28 51.2	43 33 38.5	-0.11 ± 0.04	1095	1459	7.0
TONG	Nuku'alofa, Tonga	184 49 14.8	–21 08 41.0	-1.07 ± 0.06	1154	1459	5.9
TORP	Torrance, CA, USA	241 40 09.8	33 47 52.1	-0.08 ± 0.04	939	1459	10.0
TOW2	Townsville, Australia	147 03 20.5	–19 16 09.4	-0.54 ± 0.03	939	1459	10.0
TRAB	Trabzon, Turkey	39 46 32.0	40 59 41.0	0.38 ± 0.02	1039	1455	8.0
TRDS	Trondheim, Norway	10 19 09.0	63 22 17.0	4.93 ± 0.03	1086	1459	7.2
TRO1	Tromsø, Norway	18 56 22.7	69 39 45.8	3.50 ± 0.05	948	1459	9.8
TRON	Trondheim, Norway	10 19 09.0	63 22 17.0	-9.50 ± 0.79	939	1050	2.1
TSEA	Anchorage, AK, USA	210 06 18.1	61 11 14.4	3.53 ± 0.07	1016	1459	8.5
TSKB	Tsukuba, Japan	140 05 15.0	36 06 20.5	-0.14 ± 0.05	939	1459	10.0
TUKT	Tuktoyaktuk, Canada	227 00 20.3	69 26 17.6	-0.01 ± 0.02	1233	1459	4.3
TUVA	Funafuti, Tuvalu	179 11 47.6	-8 31 31.0	-0.01 ± 0.05	1142	1459	6.1
UCLU	Ucluelet, Canada	234 27 30.1	48 55 32.3	2.82 ± 0.09	1138	1459	6.2
ULAB	Ulaanbaatar, Mongolia	107 03 08.4	47 51 54.2	0.83 ± 0.02	1087	1459	7.2
UNB1	Fredericton, Canada	293 21 29.9	45 57 00.8	0.61 ± 0.09	1123	1388	5.1
UNSA	Salta, Argentina	294 35 32.5	–24 43 38.8	-0.87 ± 0.06	1199	1459	5.0

Table 2. Continued.

Station	Name	Longitude	Latitude	Trend (mm yr^{-1})	Begin	End	Length
USNO	US Naval Obs., WA, USA	282 56 01.6	38 55 08.3	-1.67 ± 0.02	939	1459	10.0
UZHL	Uzhgorod, Ukraine	22 17 51.4	48 37 55.1	0.14 ± 0.04	1016	1459	8.5
VAAS	Vaasa, Finland	21 46 14.3	62 57 40.3	8.66 ± 0.04	999	1459	8.8
VALD	Val d'Or, Canada	282 26 09.0	48 05 49.4	8.04 ± 0.04	1148	1459	6.0
VALE	Valencia, Spain	359 39 44.5	39 28 51.0	-1.33 ± 0.06	1094	1459	7.0
VANU	Port Vila, Vanuatu	168 18 54.5	–17 44 38.3	-2.87 ± 0.06	1183	1459	5.3
VARS	Vardø, Norway	31 01 52.3	70 20 10.9	3.70 ± 0.04	1086	1459	7.2
VENE	Venice, Italy	12 19 55.1	45 26 13.1	-1.04 ± 0.05	1138	1437	5.8
VESL	Vesleskarvet, Antarctica	357 09 29.6	–71 40 25.7	0.01 ± 0.10	970	1459	9.4
VILL	Villafranca, Spain	356 02 52.9	40 26 36.9	-1.75 ± 0.03	939	1459	10.0
VIMS	Wachapreague, VA, USA	284 18 46.8	37 36 30.1	-3.13 ± 0.02	939	1459	10.0
VIS0	Visby, Sweden	18 22 02.3	57 39 13.9	3.14 ± 0.03	999	1459	8.8
VTIS	Los Angeles, CA, USA	241 42 22.2	33 42 45.5	0.46 ± 0.07	987	1459	9.1
WARN	Warnemuende, Germany	12 06 05.1	54 10 11.2	0.48 ± 0.05	1205	1459	4.9
WGTN	Wellington, NZ	174 48 21.2	–41 19 24.4	-2.64 ± 0.02	939	1459	10.0
WGTT	Wellington, NZ	174 46 53.7	–41 17 25.6	-4.22 ± 0.02	1040	1459	8.1
WILL	Williams Lake, Canada	237 49 55.9	52 14 12.7	1.92 ± 0.03	939	1459	10.0
WIS1	Wisconsin Point, WI, USA	267 59 05.2	46 42 18.2	-0.88 ± 0.05	939	1453	9.9
WLAD	Wladyslawowo, Poland	18 25 07.5	54 47 48.3	0.26 ± 0.03	1215	1459	4.7
WSRT	Westerbork, NL	6 36 16.2	52 54 52.6	-0.60 ± 0.02	939	1459	10.0
WTZR	Wettzell, Germany	12 52 44.1	49 08 39.1	-0.08 ± 0.02	939	1459	10.0
WUHN	Wuhan, China	114 21 26.1	30 31 54.0	4.66 ± 0.09	939	1459	10.0
YAKT	Yakutsk, Russia	129 40 49.1	62 01 51.5	-5.44 ± 0.34	992	1459	9.0
YAR1	Yarragadee, Australia	115 20 49.1	–29 02 47.6	-1.31 ± 0.07	939	1166	4.4
YELL	Yellowknife, Canada	245 31 09.5	62 28 51.2	6.20 ± 0.02	939	1459	10.0
YSSK	Yuzhno-Sakhalinsk, Russia	142 43 00.2	47 01 47.0	1.15 ± 0.02	1020	1459	8.4
ZECK	Zelenchukskaya, Russia	41 33 54.2	43 47 18.2	1.83 ± 0.02	939	1459	10.0
ZIMM	Zimmerwald, CH	7 27 55.0	46 52 37.6	1.67 ± 0.03	939	1459	10.0

[1] Subsidence at Aguascalientes (INEG) has been treated in Esquivel et al. (2006)

Table 3. Comparison of the vertical velocities (mm yr^{-1}) of GPS stations common in our and three recent solutions.

Station	Our solution	Santamaría-Gómez et al. (2012) solution	Bouin and Wöppelmann (2010) solution	Zhang et al. (2008) solution
ALRT	5.15 ± 0.03	6.43 ± 0.44	5.46 ± 1.64	8.96 ± 0.05
BAHR	0.53 ± 0.02	0.21 ± 0.17	0.93 ± 0.72	0.28 ± 0.01
CHUR	9.67 ± 0.03	10.36 ± 0.10	10.77 ± 0.72	10.80 ± 0.04
FTS1	2.82 ± 0.02	2.13 ± 0.34	3.00 ± 0.73	-0.89 ± 0.03
MAW1	-0.95 ± 0.01	-0.11 ± 0.21	-0.35 ± 0.72	3.20 ± 0.02
MOB1	-4.03 ± 0.05	-3.05 ± 0.39	-3.58 ± 0.76	-2.45 ± 0.04
NANO	0.60 ± 0.03	0.83 ± 0.18	1.84 ± 0.80	0.46 ± 0.01
NEAH	3.96 ± 0.02	2.63 ± 0.25	3.82 ± 0.82	2.93 ± 0.02
NEWP	1.57 ± 0.02	0.78 ± 0.35	1.61 ± 0.77	1.34 ± 0.01
NOUM	-3.06 ± 0.05	0.63 ± 0.51	-2.68 ± 0.80	-0.05 ± 0.02
NYAL	8.81 ± 0.04	8.27 ± 0.26	8.19 ± 0.73	8.32 ± 0.01
PARC	-1.26 ± 0.02	-0.15 ± 0.18	-1.39 ± 0.87	0.66 ± 0.05
PERT	-6.30 ± 0.05	-2.98 ± 0.34	-5.21 ± 0.73	-3.88 ± 0.02
PETP	-4.15 ± 0.07	-1.91 ± 0.45	-2.70 ± 0.88	-3.91 ± 0.02
SEAT	-0.20 ± 0.07	-1.34 ± 0.23	0.14 ± 0.81	-0.98 ± 0.02
SFER	1.22 ± 0.03	-0.15 ± 0.18	1.60 ± 0.89	2.00 ± 0.02
STJO	0.59 ± 0.02	-0.10 ± 0.15	-0.22 ± 0.72	-0.30 ± 0.01
SYOG	0.64 ± 0.04	2.04 ± 0.44	2.75 ± 0.80	3.45 ± 0.02
TRO1	3.50 ± 0.05	3.12 ± 0.20	3.43 ± 0.82	3.95 ± 0.02
WGTT	-4.22 ± 0.02	-2.83 ± 0.33	-3.94 ± 1.04	-1.64 ± 0.03

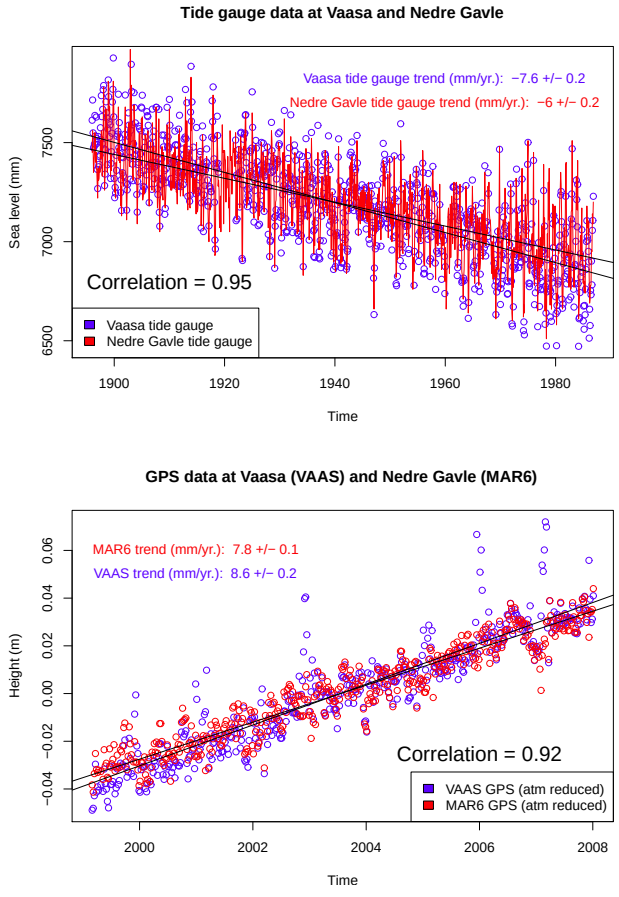

Fig. 8. The correlation of the height time series of two tide gauges Vaasa and Nedre Gavle (the upper panel) situated on the opposite sides of the Gulf of Bothnia at approximately 340 km distance. The correlation of the height time series of their co-located GPS stations, VAAS and MAR6 (with atmospheric loading correction applied, the lower panel).

both cases for the common period (1896–1986) (Fig. 9, upper panel).

4.2.3 Glacial isostatic adjustment: Canada (Churchill, CHUR, and Kuujjuarapik, KUUJ)

Both Churchill and Kuujjuarapik lie in the Hudson Bay, which is also subject to the glacial isostatic adjustment. Both GPS stations show strong secular uplift trends: $9.67 \pm 0.03\,\mathrm{mm\,yr^{-1}}$ (CHUR) and $11.52 \pm 0.06\,\mathrm{mm\,yr^{-1}}$ (KUUJ) (Fig. 10, middle panel). Despite their distance (1067 km), the two GPS stations display significant correlation ($R = 0.92$) of their height time series, also of the detrended ones ($R = 0.47$, Fig. 10, lower panel). The secular trend in the GPS data is nicely visible also in the Churchill tide gauge data. For 1940–2009, the Churchill tide gauge yields a trend of $-9.7 \pm 0.1\,\mathrm{mm\,yr^{-1}}$ ($-9.54 \pm 0.2\,\mathrm{mm\,yr^{-1}}$ with a seasonal component removed). It is clear even from the visual inspection of the Churchill tide gauge (Fig. 10, upper panel) that the overall negative regional sea level trend has flattened considerably since the beginning of the 1990s. For the 1998–2007, the trend at Churchill yields $-2.8 \pm 3.5\,\mathrm{mm\,yr^{-1}}$. Removing the seasonal signal reduces the standard error and results in a substantially larger trend estimate of $-5.18 \pm 0.97\,\mathrm{mm\,yr^{-1}}$. This means that, for 1998–2007, the full data trend is around two-thirds smaller than for the whole period of coverage, and about half when the seasonal signal is removed. An explanation for this behaviour can be found in Déry et al. (2011), who mention that there is a notable positive trend in river discharge into Hudson Bay, starting around the 1990s and continuing until 2008, the end of their time series. At the same time, there is a shift in the seasonality of river discharge into the bay. With a positive trend in winter and negative trend in summer streamflow, the time series variance is expected to increase. This explains the large impact of the seasonal signal on the trend for the 1998–2007 time series. The tide gauge signal, which has long been dominated by GIA, is apparently now influenced much more strongly by the changing hydrological processes in Hudson Bay.

4.2.4 Bogotá (BOGT), Colombia

This station is a peculiar example. It is located near the building of the Instituto Geográfico Agustín Codazzi (IGAC) in Bogotá and has been continuously subsiding during the past years. The station was treated in Kaniuth et al. (2001) together with another station, BOGA, which is positioned on the top of the IGAC building. In their treatment, the authors suggest that construction work may have worsened the subsidence processes caused by sedimentation in the area. The vertical trend at BOGT has almost doubled since it was first estimated in their 2001 paper ($-25.2 \pm 1.4\,\mathrm{mm\,yr^{-1}}$), now reaching the alarming rate of $-44.21 \pm 0.19\,\mathrm{mm\,yr^{-1}}$ (Fig. 11). Obviously, the station cannot be used for any purposes within the TIGA framework.

4.3 Stations with height trend changes

4.3.1 Trend changes in GPS station data: Arequipa (AREQ), Peru

Arequipa lies in southwestern Peru, in the subduction zone where the oceanic Nazca plate is subducted under the South American plate along the Peru–Chile trench. It is an interesting example of a trend change, as the station recorded the 2001 Arequipa–Camana–Tacna area (M:8.4W) earthquake (Utsu, 1990) and its effects on land movement. The trend change is visible in the time series (Fig. 12) from GPS week 1120 (25 June 2001), two days after the date of the earthquake on 23 June 2001. Before the event, the trend was $-2.6 \pm 0.5\,\mathrm{mm\,yr^{-1}}$, changing direction to a positive $4.2 \pm 0.1\,\mathrm{mm\,yr^{-1}}$ uplift trend afterwards. From 2005 on, a slight trend reduction can be observed. This is consistent

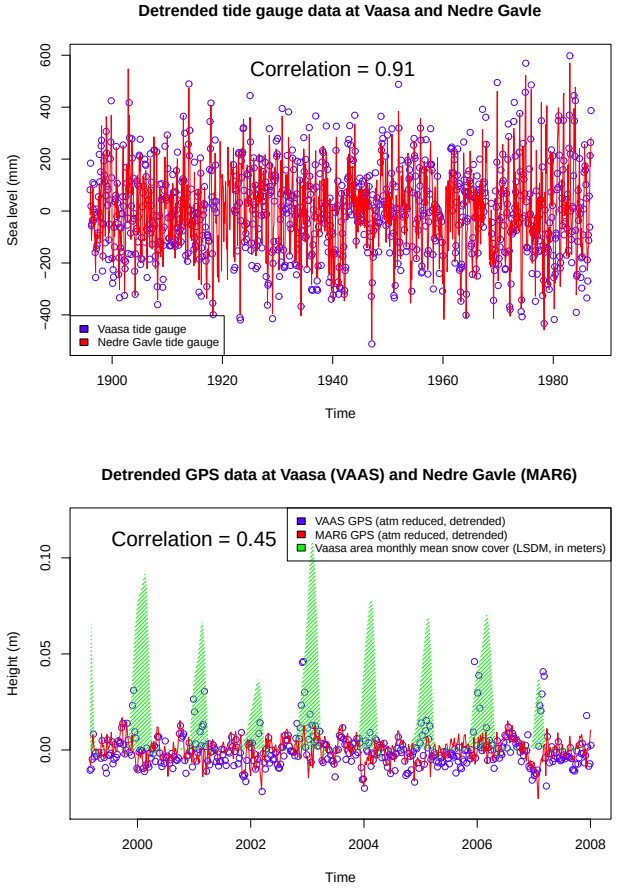

Fig. 9. The upper panel: the detrended sea level time series for tide gauges Vaasa and Nedre Gavle for the common period (1896–1986). The lower panel: the detrended height time series for the co-located GPS stations Vaasa (VAAS) and Nedre Gavle (MAR6). The green shading depicts the modelled mean snow cover at the four neighbouring grid points surrounding the station according to the LSDM hydrology model.

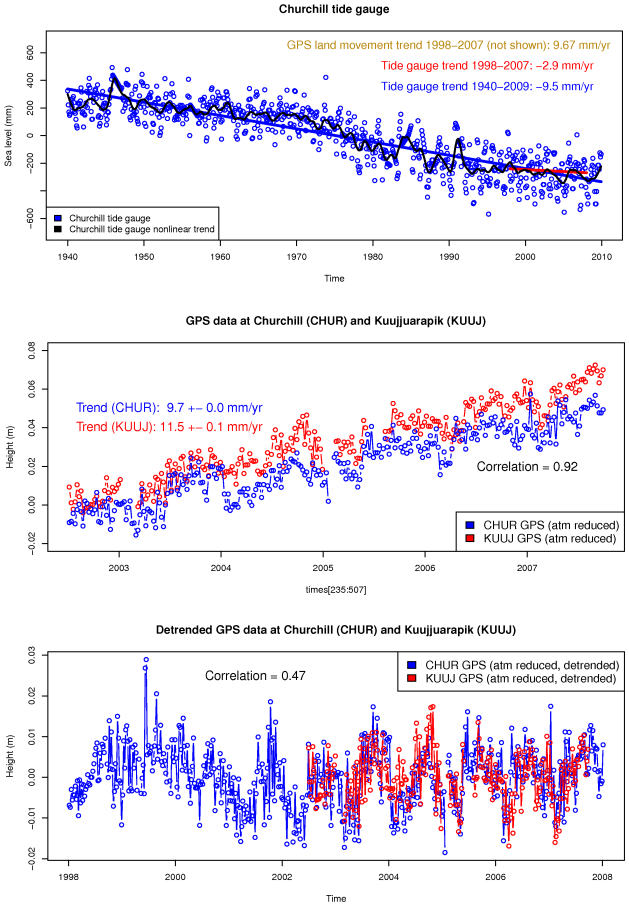

Fig. 10. The upper panel: sea level time series at tide gauge at Churchill; the middle panel: height time series and trends at GPS stations CHUR (Churchill) and KUUJ (Kuujjuarapik); the lower panel: detrended height time series at these GPS stations.

with exponential behaviour that can be expected for a post-seismic event.

4.3.2 Trend change in tide gauge data: Kushimoto (P208), Japan

Kushimoto (GPS station P208) is located at the southern tip of the Kii Peninsula, Wakayama prefecture. It is situated within the Nankai trough subduction zone and was affected, among others, by the 1946 Nankai earthquake (M = 8) (Utsu, 1990). Sato et al. (1998) mention that, prior to the 1944 earthquake, the southern part of the peninsula is supposed to have subsided with a constant rate of 5–6 mm yr^{-1}. The Kushimoto tide gauge record indicates a clear trend change coinciding with the minor (M = 5.6) Wakayama prefecture earthquake of 9 May 1987 (Utsu, 1990). The relative sea level trend from the tide gauge before the earthquake is a moderate $+0.6 \pm 0.2$ mm yr^{-1}, increasing by almost ten times to $+6.5 \pm 0.2$ mm yr^{-1} after the earthquake. The vertical land movement trend determined from the GPS station P208 over the 2005–2010 period is -6.3 ± 0.1 mm yr^{-1}. A comparison with the TOPEX/Poseidon (1994–2001) sea level anomaly trend (-1.8 ± 1.7 mm yr^{-1}) strengthens the assumption that the major part of the tide gauge trend is caused by the land movement (Fig. 13).

Apparently, after the 1987 earthquake, the southern part of the Kii peninsula resumed its original subsiding motion. Still, (Isoda et al., 2004) remarked that the Kushimoto tide gauge is located on the (uplifting) Eurasia plate. Emery and Aubrey (1991) mentioned submergence caused by groundwater extraction as another possible cause for subsidence.

4.3.3 Trend change in tide gauge and GPS data: Aburatsu (P211), Japan

Another example of a trend change is Aburatsu tide gauge located at Nichinan, Miyazaki prefecture, Japan. One trend

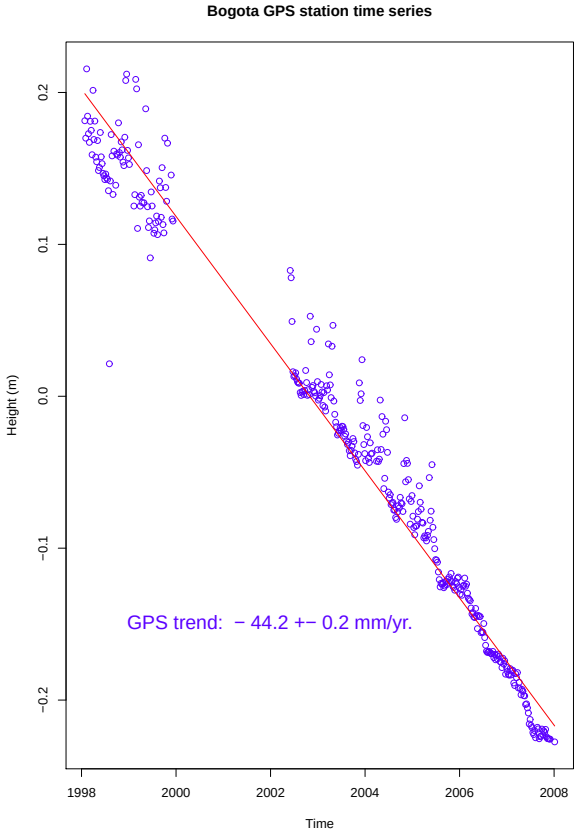

Fig. 11. GPS station Bogotà (BOGT) exhibits a significant secular height trend of $-44.2 \pm 0.2\,\mathrm{mm\,yr^{-1}}$.

change (Fig. 14, upper panel) occurs in the aftermath of the July, 1970 Miyazaki prefecture earthquake (M = 6.7). Another trend change occurs in April 1984 and coincides with the Kagoshima prefecture earthquake of 28 April 1986 (M = 4.4) (Utsu, 1990).

An analysis of the height time series for the co-located GPS station P211 shows (Fig. 14, lower panel) a trend change from GPS week 1342 (26 September 2005). Before this (May 2003–May 2005), the land movement trend from the GPS time series with a value of $-3.3 \pm 0.6\,\mathrm{mm\,yr^{-1}}$ explains a large part of the sea level rise trend of $3.5 \pm 1.0\,\mathrm{mm\,yr^{-1}}$ computed for the time after the last trend change (from April 1987). After the 2005 trend change, the land movement switches sign to $2.1 \pm 0.7\,\mathrm{mm\,yr^{-1}}$. Drops in the time series as depicted in Fig. 14 clearly mark the impact of the Oita 2006 (12 June, M = 6.2) and 2007 (6 June, M = 4.9) earthquakes. The impact of the 2005 Fukuoka earthquakes (Utsu, 1990) (20 and 22 March, 20 April, and 5 May) is less clear, but the trend change begins a few weeks after the earthquake.

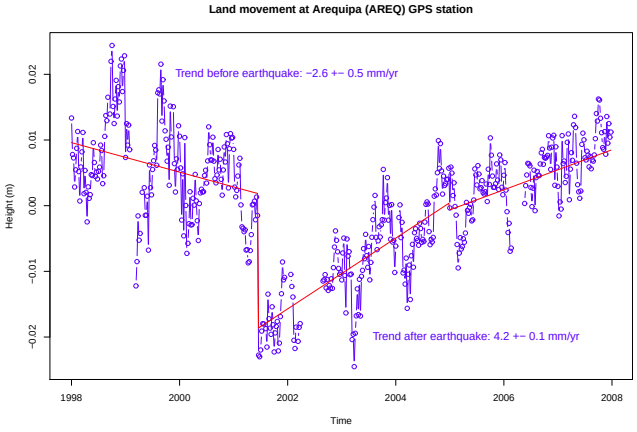

Fig. 12. The height trend change at GPS station Arequipa (AREQ) from $-2.6 \pm 0.5\,\mathrm{mm\,yr^{-1}}$ to $+4.2 \pm 0.1\,\mathrm{mm\,yr^{-1}}$ caused by the 2001 Arequipa–Camana–Tacna area earthquake.

4.3.4 Variations caused by hydrological processes: Brasilia (BRAZ), Brazil

The time series of this GPS station (Fig. 15) situated in the Roncador Ecological Reserve, approximately 35 km south of Brasilia, exhibits strong annual variations from hydrological effects. Van Dam et al. (2001) already mention BRAZ as an example for strong annual variations due to hydrological water loading, although, at the time of publication, there was only a short time series available.

To separate the atmospheric pressure loading effects from the hydrological variations, a pressure correction was applied following van Dam et al. (1994). NCEP 6-hourly surface pressure data were convolved with Farrell's Green's functions using the programme provided on Tonie van Dam's website (van Dam, 2010) and the technique outlined in van Dam et al. (1994).

From 2006 on, a strong negative trend is visible in the GPS time series. This decrease can be also found in GRACE data (Kurtenbach et al., 2009). For the comparison, the GRACE data were resampled to monthly values and filtered, then converted to equivalent water height. The gridded product was provided by Henryk Dobslaw, GFZ. For a qualitative comparison, the GRACE water column data are scaled by factor 150 in Fig. 15. The comparison with water mass data from the LSDM model (Dill, 2008) also shows a strong decrease in water column height. The cause of the subsidence is apparently the drought that hit this region in late summer and fall of 2006 (EM-DAT, 2011).

4.4 Stations with zero height trend

Tuktoyaktuk (TUKT) station in northwestern Canada is an example for a site with a height trend very close to zero ($-0.01 \pm 0.02\,\mathrm{mm\,yr^{-1}}$). Located close to the Alaskan border, the station is apparently affected neither by the positive

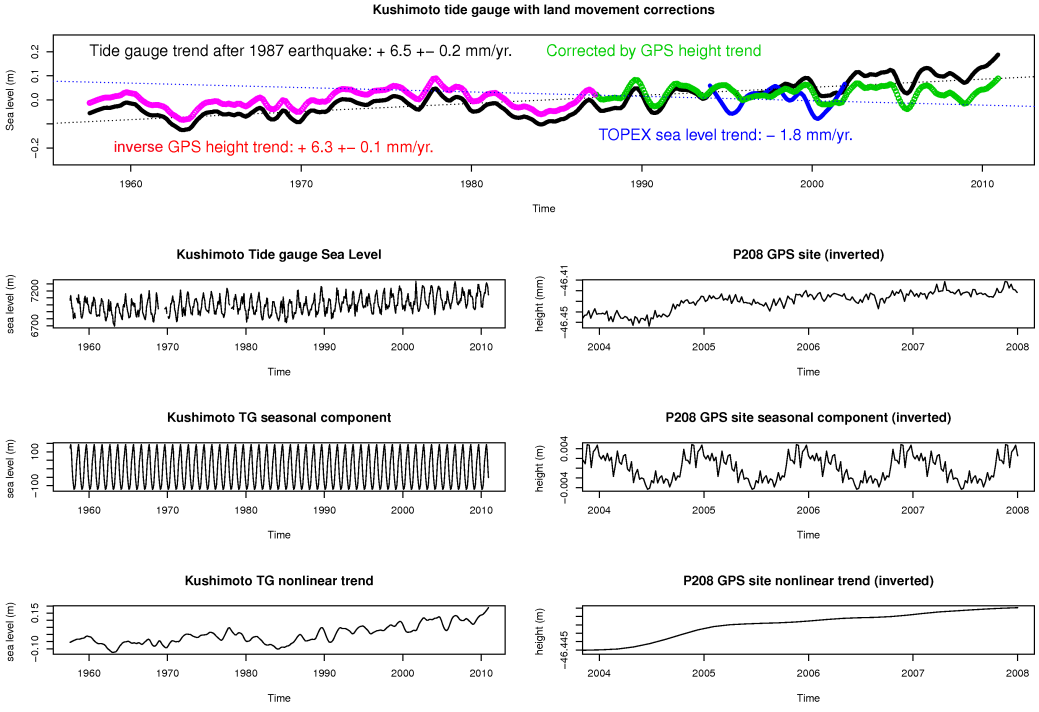

Fig. 13. The apparent sea level rise ($+6.5 \pm 0.2\,\mathrm{mm\,yr^{-1}}$) at Kushimoto tide gauge after the 1987 Wakayama prefecture earthquake and its comparison with the height trend ($-6.3 \pm 0.1\,\mathrm{mm\,yr^{-1}}$) at the co-located GPS station P208.

GIA signal centered on Eastern Canada, nor by the land movement signals caused by the recent ice loss (Larsen et al., 2004) commonly found in south Alaska. The moderate length of the time series (4.3 yr), however, makes this assessment a preliminary one. The seasonal cycle produces a spurious trend ($0.5 \pm 0.3\,\mathrm{mm\,yr^{-1}}$), if not removed (Fig. 16).

Some more GPS stations with longer time series demonstrate the height trend being very close to zero. These are, for example, GPS station CKIS (Rarotonga, Cook Islands, in free association with New Zealand) with the height trend of $0.04 \pm 0.03\,\mathrm{mm\,yr^{-1}}$ obtained over the 6.3 yr time series; PLO3 (Point Loma, CA, USA) for which the vertical velocity of $-0.01 \pm 0.09\,\mathrm{mm\,yr^{-1}}$ was computed at the 8.5-yr time interval; RWSN (Rawson, Argentina) with the height trend of $-0.01 \pm 0.02\,\mathrm{mm\,yr^{-1}}$ calculated at the 7.9-yr time span; TUVA (Funafuti, Tuvalu) for which the vertical velocity of $-0.01 \pm 0.05\,\mathrm{mm\,yr^{-1}}$ was estimated using the 6.1-yr time series and some other stations.

5 Discussion

The linear height trends obtained in this work have been compared with previous solutions. Thus, our solution (Table 2) contains linear height trends additionally for the following 38 GPS stations not present in the previous GFZ solution (Zhang et al., 2008) due to the inclusion of GPS data from these stations located in Brazil, Canada, Iceland, Israel, Japan, Norway, Poland, Spain, Sweden, Tasmania, Turkey, the USA and on Tahiti in the GT1 solution: 0194, ANDE, ANDO, ANTA, BUR1, CSAR, NCDK, NEIA, P102, P103, P104, P108, P109, P110, P112, P114, P115, P116, P117, P118, P119, P120, P124, P201, P202, P203, P204, P206, P209, P211, P212, P213, PAPE, PLUZ, REYZ, SKE0, TUKT, VTIS, WLAD. This is a notable contribution to the densification of the GPS station network processed.

We have compared the vertical velocities of our solution with the previous GFZ solution (Zhang et al., 2008) obtained by processing GPS data from a global network of 370 GPS stations from January 1994 till December 2006 and containing the vertical velocities of 335 stations aligned to ITRF2000 (Altamimi et al., 2002) and two solutions of Université de La Rochelle: ULR3 solution (Bouin and Wöppelmann, 2010) derived using GPS data from a global network of 227 stations from January 1997 to November 2006 and containing the vertical velocities of 180 stations expressed in ITRF2005 and ULR5 solution (Santamaría-Gómez et al., 2012) obtained by processing GPS data from a global network of 420 stations from January 1995 to December 2010 and providing the vertical velocities for 326 stations given in ITRF2008. Both ULR solutions use IGS absolute phase centre corrections for both tracking and transmitting antennas, as our (GT1) solution does, whereas the previous GFZ solution was computed using relative phase

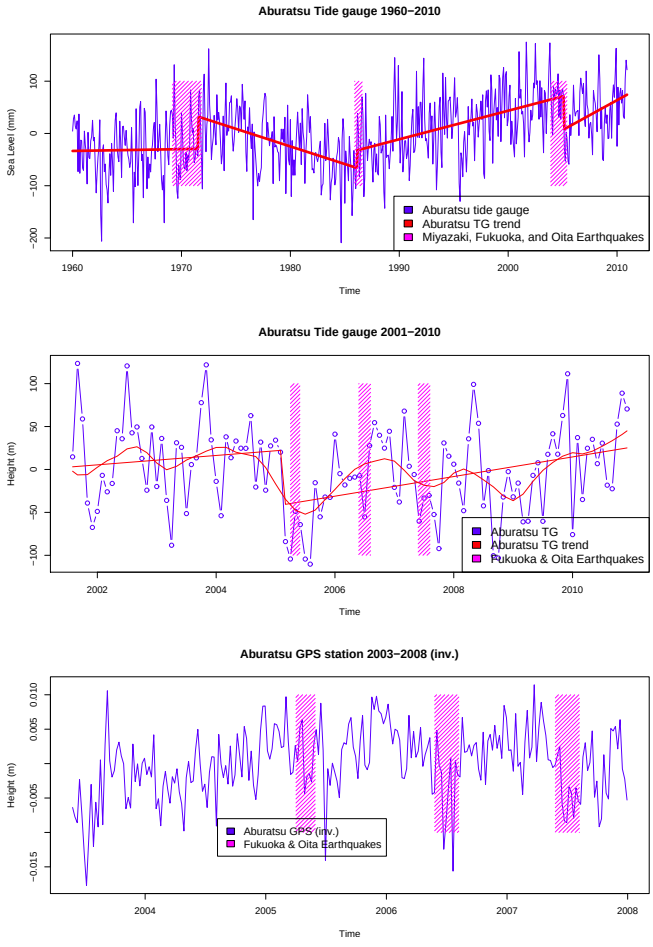

Fig. 14. The impact of earthquakes on Aburatsu tide gauge and co-located GPS station P211 height time series: Aburatsu tide gauge sea level time series (1960–2010, the upper panel), a close-up of the tide gauge time series for 2001–2010 (the middle panel) and inverted height time series at the GPS station P211 (2003–2008, the lower panel). The pink shading marks the interval for possible breakpoints detected by the BFAST algorithm caused by the 2005 Fukuoka earthquakes and the 2006 and 2007 Oita earthquakes.

centre corrections and some obsolete models. The comparison shows that the discrepancies in the vertical velocities are below 1 mm yr^{-1} for 106 of 142 common stations (i.e. about 75 per cent) for GT1 and ULR3 solutions, for 120 of 179 common stations (i.e. about 67 per cent) for GT1 and ULR5 solutions, whereas only for 101 of 224 common stations (i.e. about 45 per cent) for GT1 and Zhang et al. (2008) solutions due to the use of some obsolete models, in particular, relative phase centre corrections in the previous GFZ solution. The vertical velocities of GPS stations common in our and three recent solutions are provided in Table 3.

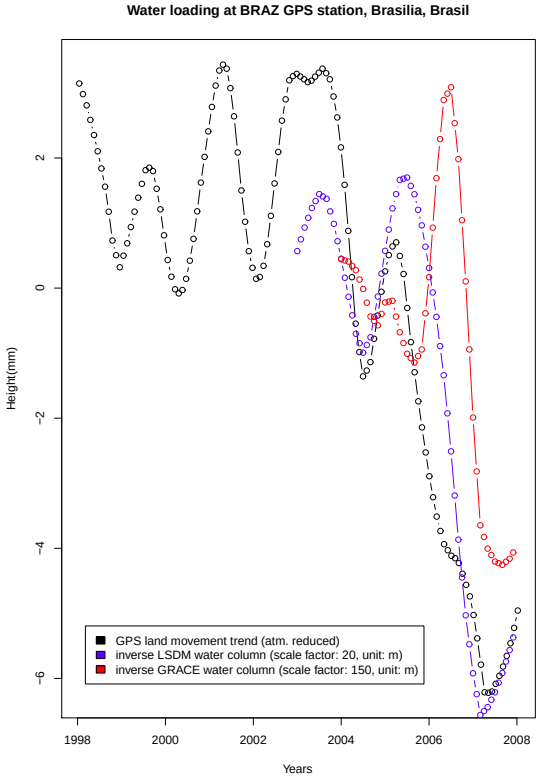

Fig. 15. A qualitative comparison of three different signals showing the 2006 drought in Brazil: height time series of GPS station Brasilia (BRAZ), inverse water storage mass and inverse hydrological loading from GRACE data. The nonlinear trend (seasonal signal and noise removed) is depicted in all three time series. Different scale factors are used for three plots.

6 Conclusions

We have reprocessed GPS data from a global network of 403 GPS stations over the 10-yr time span (1998–2007) using new models and algorithms and derived time series of weekly coordinates of these stations. The station coordinate repeatabilities of daily solutions with respect to the weekly ones reach 1 mm in the north and east components and 3 mm in the up component. The standard deviations of the north and east coordinate residual weighted average of our solution with respect to those of the IG1 combined solution of the first IGS data reprocessing campaign are about 1–2 mm and those of the up component are about 3–4 mm for the whole time span. Vertical velocities of GPS stations having a tracking history longer than 2.5 yr were computed and compared with the estimates from tide gauge data and some other GPS-derived solutions. Some examples of different types of station vertical velocities such as prominent secular height trend, trend changes caused by various geophysical processes and zero height trend are presented and discussed. The comparison of the vertical velocities of GPS stations of our solution with those of some other solutions including the recent (ULR3

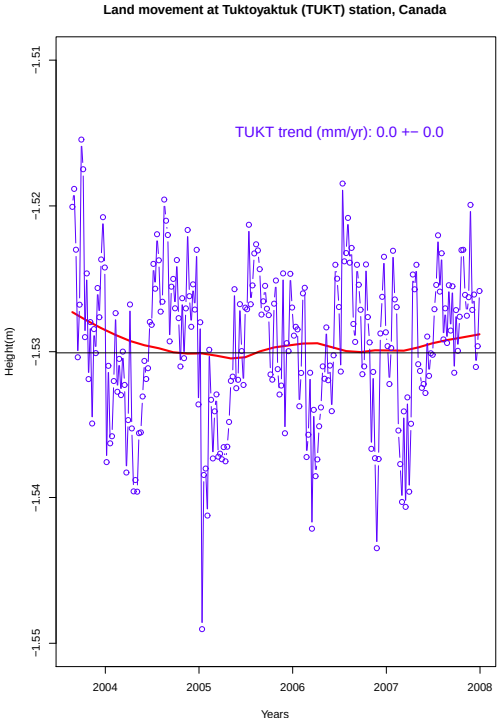

Fig. 16. The Canadian GPS station Tuktoyaktuk has close to zero height trend over the years 2003.7–2008.0.

and ULR5) solutions of Université de La Rochelle indicates that the accuracy of the vertical velocities is below 1 mm yr^{-1} for the most GPS stations of our solution. The height time series for the GPS stations co-located at tide gauges and vertical velocities at these stations can be used to correct the estimates of regional and global sea level changes based on tide gauge data. It is planned to perform a new reprocessing of continuous GPS data at longer time span (1994–2011) for an increased number of GPS stations at tide gauges by using newer models and ITRF2008 as a priori terrestrial reference frame within the second IGS data reprocessing campaign. This will allow computation of a longer time series of station coordinates for a larger number of GPS stations with an increased accuracy of vertical velocity.

Acknowledgements. GPS data available from IGS, TIGA and some other stations and agencies were used in this study. The research was supported by German Ministry of Education and Research (BMBF) within the GEOTECHNOLOGIEN geoscientific *R&D* programme (SEAVAR Project). The study described in Sect. 4 was performed by N. Schön. The authors are grateful to T. Schöne (GFZ) for useful discussions, K. Snopek (GFZ) for some advices related to LaTeX use, the reviewers (J.R. Ray, A. Santamaría-Gómez and anonymous one) and topical editor C. Gaina for their valuable comments and suggestions that improved the paper.

Edited by: C. Gaina

References

Altamimi, Z., Collilieux, X., Legrand, J., Garayt, B., and Boucher, C.: ITRF2005: A new release of the International Terrestrial Reference Frame based on time series of station positions and Earth Orientation Parameters, J. Geophys. Res., 112, B09401, doi:10.1029/2007JB004949, 2007.

Altamimi, Z., Collilieux, X., and Métivier, L.: ITRF2008: an improved solution of the international terrestrial reference frame, J. Geodesy, 85, 457–473, doi:10.1007/s00190-011-0444-4, 2011.

Altamimi, Z., Sillard, P., and Boucher, C.: ITRF2000: A new release of the International Terrestrial Reference Frame for earth science applications, J. Geophys. Res., 107(B10), 2214, doi:10.1029/2001JB000561, 2002.

Bar-Sever, Y. E.: A new model for GPS yaw attitude, J. Geodesy, 70, 714–723, doi:10.1007/BF00867149, 1996.

Beutler, G., Brockmann, E., Hugentobler, U., Mervart, L., Rothacher, M., and Weber, R.: Combining consecutive short arcs into long arcs for precise and efficient GPS orbit determination, J. Geodesy, 70, 287–299, doi:10.1007/BF00867349, 1996.

Blewitt, G. and Lavallée, D.: Effect of annual signals on geodetic velocity, J. Geophys. Res., 107, B7, 2145, doi:10.1029/2001JB000570, 2002.

Boehm, J., Niell, A. E., Tregoning, P., and Schuh, H.: Global Mapping Functions (GMF): a new empirical mapping function based on numerical weather model data, Geophys. Res. Lett., 33, L07304, doi:10.1029/2005GL025546, 2006.

Boehm, J., Heinkelmann, R., and Schuh, H.: Short Note: a global model of pressure and temperature for geodetic applications, J. Geodesy, 81, 679–683, doi:10.1007/s00190-007-0135-3, 2007.

Bouin, M. N. and Wöppelmann, G.: Land motion estimates from GPS at tide gauges: a geophysical evaluation, Geophys. J. Int., 180, 193–209, doi:10.1111/j.1365-246X.2009.04411.x, 2010.

Buble, G., Bennett, R. A., and Hreinsdóttir, S.: Tide gauge and GPS measurements of crustal motion and sea level rise along the eastern margin of Adria, J. Geophys. Res., 115, B02404, doi:10.1029/2008JB006155, 2010.

Cleveland, R. B., Cleveland, W. S., McRae, J. E., and Terpenning, I.: STL: A seasonal-trend decomposition procedure based on Loess, Journal of Official Statistics, 6, 3–73, 1990.

Collilieux, X. and Wöppelmann, G.: Global sea-level rise and its relation to the terrestrial reference frame, J. Geodesy, 85, 9–22, doi:10.1007/s00190-010-0412-4, 2011.

Collilieux, X., Métivier, L., Altamimi, Z., van Dam, T., and Ray, J.: Quality assessment of GPS reprocessed terrestrial reference frame, GPS Solut., 15, 219–231, doi:10.1007/s10291-010-0184-6, 2011.

Déry, S. J., Mlynowski, T. J., Hernández-Henríquez, M. A., and Straneo, F.: Interannual variability and interdecadal trends in Hudson Bay streamflow, J. Marine Syst., 88, 341-351, doi:10.1016/j.jmarsys.2010.12.002, 2011.

Dill, R.: Hydrological model LSDM for operational Earth rotation and gravity field variations, Scientific Technical Report, GFZ Potsdam, STR08/09, 37 pp., doi:10.2312/GFZ.b103-08095, 2008.

Dow, J.M., Neilan, R.E., and Rizos, C.: The international GNSS Service in a changing landscape of Global Navigation Satellite Systems, J. Geodesy 83, 191–198, doi:10.1007/s00190-008-0300-3, 2009.

EM-DAT: The OFDA/CRED International Disaster Database, Université Catholique de Louvain, Belgium, Brussels, available at: http://www.emdat.be, 2011.

Emery, K. O. and Aubrey, D. G.: Sea levels, land levels, and tide gauges, Springer, New York, 1991.

Esquivel, R., Hernández, A., and Zermeño, M.E.: GPS for Subsidence Detection, the Case Study of Aguascalientes, in: Geodetic Deformation Monitoring: from Geophysical to Engineering Roles, International Association of Geodesy Symposia, Springer, 131, 254–258, doi:10.1007/978-3-540-38596-7_31, 2006.

Fu, Y., Freymueller, J. T., and van Dam, T.: The effect of using inconsistent ocean tidal loading models on GPS coordinate solutions, J. Geodesy, 86, 409–421, doi:10.1007/s00190-011-0528-1, 2012.

Ge, M., Gendt, G., Dick, G., and Zhang, F. P.: Improving carrier-phase ambiguity resolution in global GPS network solutions, J. Geodesy, 79, 103–110, doi:10.1007/s00190-005-0447-0, 2005.

Ge, M., Gendt, G., Dick, G., Zhang, F. P., and Rothacher, M.: A new data processing strategy for huge GNSS global networks, J. Geodesy, 80, 199–203. doi:10.1007/s00190-006-0044-x, 2006.

Gendt, G., Dick, G., Mai, W., Nischan, T., and Sommerfeld, W.: Nutzerhandbuch zum Programmsystem EPOS. P.V2 (Earth Parameters and Orbit determination System) für die Analyse von GPS-Daten, GeoForschungsZentrum Potsdam, Bereich "Rezente Kinematik und Dynamik der Erde", 18 February 1994.

Goebell, S. and King, M. A.: Effects of azimuthal multipath asymmetry on long GPS coordinate time series, GPS Solut., 15, 287–297, doi:10.1007/s10291-011-0227-7, 2011.

Isoda, Y., Kitamura, F., and Murakami, T.: Interannual variations of the yearly mean sea level around the Japanese islands, Bulletin of Fisheries Sciences, Hokkaido University, 55, 85–95, ISSN:1346-1842, 2004.

Kaniuth, K., Häfele, P., and Sánchez, L.: Subsidence of the permanent GPS station Bogotá, in: Vertical Reference Systems. IAG Symposia, edited by: Drewes, H., Dodson, A., Fortes, L. P., Sánchez, L., and Sandoval, P., Springer, 124, 56–59, 2002.

King, M. A., Bevis, M., Wilson, T., Johns, B., and Blume, F.: Monument-antenna effects on GPS coordinate time series with application to vertical rates in Antarctica, J. Geodesy, 86, 53–63, doi:10.1007/s00190-011-0491-x, 2012.

King, M. A. and Watson, C. S.: Long GPS coordinate time series: multipath and geometry effects, J. Geophys. Res., 115, B04403, doi:10.1029/2009JB006543, 2010.

Kurtenbach, E., Mayer-Gürr, T., and Eicker, A.: Deriving daily snapshots of the Earth's gravity field from GRACE L1B data using Kalman filtering, Geophys. Res. Lett., 36, L17102, doi:10.1029/2009GL039564, 2009.

Larsen, C. F., Motyka, R. J., Freymueller, J. T., Echelmeyer, K. A., and Ivins, E. R.: Rapid uplift of southern Alaska caused by recent ice loss, Geophys. J. Int., 158, 1118–1133, doi:10.1111/j.1365-246X.2004.02356.x, 2004.

McCarthy, D. D. and Petit, G. (eds.): IERS Conventions (2003), IERS Technical Note 32, 127 pp., ISBN 3-89888-884-3, 2004.

Munekane, H. and Boehm, J.: Numerical simulation of troposphere-induced errors in GPS-derived geodetic time series over Japan, J. Geodesy, 84, 405–417, doi:10.1007/s00190-010-0376-4, 2010.

Sánchez, L. and Bosch, W.: The role of the TIGA project in the unification of classical height systems, in: Geodetic Reference Systems, edited by: Drewes H., IAG Symposia, vol. 134, Springer, 285–290, doi:10.1007/978-3-642-00860-3_44, 2009.

Santamaría-Gómez, A., Gravelle, M., Collilieux, X., Guichard, M., Martín Míguez, B., Tiphaneau, P., and Wöppelmann, G.: Mitigating the effects of vertical land motion in tide gauge records using a state-of-the-art GPS velocity field, Global Planet, 98-99, 6–17, doi:10.1016/j.gloplacha.2012.07.007, 2012.

Sato, T., Mochizuki, K., Kasahara, J., Fujie, G., Nishisaka, H., and Koresawa, S.: Depth variation of the crustal structure of the subducting plate along the Nankai Trough, off Kii Channel, Japan, Geophys. Res. Lett., 25, 21, 4011–4014, doi:10.1029/1998GL900104, 1998.

Schmid, R., Steigenberger, P., Gendt, G., Ge, M., and Rothacher, M.: Generation of a consistent absolute phase-center correction model for GPS receiver and satellite antennas, J. Geodesy, 81, 781–798, doi:10.1007/s00190-007-0148-y, available at: ftp://igscb.jpl.nasa.gov/pub/station/general/igs05.atx, last access: 15 January 2009, 2007.

Schöne, T., Schön, N., and Thaller, D.: IGS tide gauge benchmark monitoring pilot project (TIGA): scientific benefits, J. Geodesy, 83, 249–261, doi:10.1007/s00190-008-0269-y, 2009.

Utsu, T.: Catalog of Damaging Earthquakes in the World (Through 1989), Utsu, Tokuji, Tokyo, 243 pp., 1990.

van Dam, T., Wahr, J., Milly, P. C. D., Shmakin, A. B., Blewitt, G., Lavallée, D., and Larson, K. M.: Crustal displacements due to continental water loading, Geophys. Res. Lett., 28, 651–654, doi:10.1029/2000GL012120, 2001.

van Dam, T. M.: NCEP derived 6-hourly, global surface displacements at 2.5×2.5 degree spacing, updated October 2010, available at: http://geophy.uni.lu/ncep-loading.html, last access: 23 February 2012.

van Dam, T. M., Blewitt, G., and Heflin, M. B.: Atmospheric pressure loading effects on Global Positioning System coordinate determinations, J. Geophys. Res., 99, 23939–23950, doi:10.1029/94JB02122, 1994.

Verbesselt, J., Hyndman, R., Newnham, G., and Culvenor, D.: Detecting trend and seasonal changes in satellite image time series, Remote Sens. Environ., 114, 106–115, doi:10.1016/j.rse.2009.08.014, 2010.

Verdonck, D.: Contemporary vertical crustal deformation in Cascadia, Tectonophysics, 417, 221–230, doi:10.1016/j.tecto.2006.01.006, 2006.

Williams, S. D. P. and Penna, N. T.: Non-tidal ocean loading effects on geodetic GPS heights, Geophys. Res. Lett., 38, L09314, doi:10.1029/2011GL046940, 2011.

Wöppelmann, G., Letetrel, C., Santamaria, A., Bouin, M.-N., Collilieux, X., Altamimi, Z., Williams, S. D. P., and Martin Miguez, B.: Rates of sea-level change over the past century in a geocentric reference frame Geophys. Res. Lett., 36, L12607, doi:10.1029/2009GL038720, 2009.

Wöppelmann, G., Martin Miguez, B., Bouin, M.-N., and Altamimi, Z.: Geocentric sea-level trend estimates from GPS analyses at relevant tide gauges world-wide, Global Planet. Change, 57, 396–406, doi:10.1016/j.gloplacha.2007.02.002, 2007.

Woodworth, P. L. and Player, R.: The Permanent Service for Mean Sea Level: an update to the 21st century, J. Coastal Res., 19, 287-295, 2003.

Wu, J. T., Wu, S. C., Hajj, G. A., Bertiger, W. I., and Lichten, S. M.: Effects of antenna orientation on GPS phase, Manuscr. Geodaet, 18, 91–98, 1993.

Zhang, F. P., Gendt, G., and Ge, M.: GPS Data Processing at GFZ for Monitoring the Vertical Motion of Global Tide Gauge Benchmarks, GeoForschungsZentrum Potsdam Scientific Technical Report STR07/02, 28 pp., doi:10.2312/GFZ.b103-07025, 2007.

Zhang, F. P., Wünsch, J., van Dam, T., Gendt, G., Ge, M., and Schöne, T.: Vertical Crustal Motion at Tide Gauges Derived by Analyzing GPS Time Series, GeoForschungsZentrum Potsdam Scientific Technical Report STR08/03, 106 pp., doi:10.2312/GFZ.b103-08037, 2008.